

## Anthropogenic forcing has impacted precipitation variability in the North China Monsoon Marginal Region

Xiaoen Zhao<sup>a,b</sup>, Chenxi Xu<sup>c,d</sup>, Feng Chen<sup>a,b,e,\*</sup>, Étienne Boucher<sup>f</sup>, Martín Hadad<sup>g</sup>, Fidel A. Roig<sup>h,i</sup>, Jiafeng Xu<sup>a</sup>, Mao Hu<sup>a,b</sup>, Shijie Wang<sup>a</sup>, Heli Zhang<sup>a</sup>, Youping Chen<sup>a</sup>, Weipeng Yue<sup>a</sup>, Honghua Cao<sup>a,b</sup>

<sup>a</sup> Yunnan Key Laboratory of International Rivers and Transboundary Eco-Security, Institute of International Rivers and Eco-Security, Yunnan University, Kunming 650504, China

<sup>b</sup> Southwest United Graduate School, Yunnan University, Kunming 650504, China

<sup>c</sup> State Key Laboratory of Lithospheric and Environmental Coevolution, Institute of Geology and Geophysics, Chinese Academy of Sciences, Beijing 100029, China

<sup>d</sup> College of Earth and Planetary Sciences, University of Chinese Academy of Sciences, Beijing 100049, China

<sup>e</sup> Key Laboratory of Tree-ring Physical and Chemical Research of the Chinese Meteorological Administration/Xinjiang Laboratory of Tree-ring Ecology, Institute of Desert Meteorology, Chinese Meteorological Administration, Urumqi 830002, China

<sup>f</sup> Department of Geography, GEOTOP and Centre d'études nordiques, Université du Québec à Montréal, Montréal, Québec, Canada

<sup>g</sup> Laboratorio de Dendrocronología de Zonas Áridas-Instituto y Museo de Ciencias Naturales, Universidad Nacional de San Juan, CIGEOBIO (CONICET-UNSJ), San Juan, Argentina

<sup>h</sup> Laboratorio de Dendrocronología e Historia Ambiental, IANIGLA-CCT CONICET-Universidad Nacional de Cuyo, Mendoza, Argentina

<sup>i</sup> Hémera Centro de Observación de La Tierra, Escuela de Ingeniería Forestal, Facultad de Ciencias, Universidad Mayor, Huechuraba, Santiago, Chile



### ARTICLE INFO

**Editor:** Dr. Howard Falcon-Lang

**Keywords:**

Anthropogenic forcing  
Climate system  
Tree ring  
Precipitation variability  
North China

### ABSTRACT

The Asian Summer Monsoon (ASM) is a crucial driver of precipitation, sustaining ecological balance and socio-economic development in North China. However, the extent to which climate change has influenced this monsoonal system, leading to detectable and attributable modifications in precipitation regimes, remains unclear. Here, we present a robust annual precipitation reconstruction spanning 1770–2020, using  $\delta^{18}\text{O}$  from tree ring cellulose and a simple linear regression model in the North China Monsoon Marginal Region (NCMMR). Reconstructed precipitation and independent hydroclimatic records reveal a pronounced drying trend across the NCMMR since the 1950s. Multiple linear regression modelling, water vapor transport analyses using ensemble means from the Community Earth System Model-Last Millennium Ensemble, and correlation analysis indicate that precipitation variability in the NCMMR is modulated by the Indian Ocean Dipole, El Niño-Southern Oscillation, Atlantic Multidecadal Oscillation, and Interdecadal Pacific Oscillation. Nevertheless, fingerprint analysis suggests that the observed precipitation decline since the 1950s is strongly associated with greenhouse gas concentrations, albeit partially offset by the effects of anthropogenic aerosol emissions and internal variability. The impact of greenhouse gas forcing on precipitation variability is expected to intensify in the coming decades.

### 1. Introduction

The transitional zone between semi-arid and semi-humid climates in North China is particularly sensitive to global climate change due to its ecologically fragile environment (Ding et al., 2022; Wang et al., 2020a). East and South Asia experience pronounced seasonal hydroclimatic variability governed by the Asian Summer Monsoon (ASM) system, with atmospheric circulation regulating precipitation dynamics on both

interannual and interdecadal timescales (Kathayat et al., 2022; Sha et al., 2023; Chen et al., 2024). Ongoing global warming poses significant risks and challenges to ecological sustainability and socio-economic development, particularly as extreme climatic events driven by potential monsoon instability become increasingly frequent (Buckley et al., 2014; Chen et al., 2022; Singh et al., 2014; Turner and Annamalai, 2012; Yang et al., 2021; Xu et al., 2023a, 2023b; Wu et al., 2025). Although post-industrial changes in extreme precipitation and drought events

\* Corresponding author at: Yunnan Key Laboratory of International Rivers and Transboundary Eco-Security, Institute of International Rivers and Eco-Security, Yunnan University, Kunming 650504, China.

E-mail address: [feng653@163.com](mailto:feng653@163.com) (F. Chen).

have been attributed to the complex interactions between natural variability and anthropogenic influences, assessing the underlying drivers of climate change in monsoon marginal regions remains inherently challenging (Liu et al., 2016; Song et al., 2014; Zhang, 2015).

Hydroclimatic reconstructions and simulation studies at the global scale have utilised a diverse range of proxy data sources, including lake sediments, historical records, speleothems, tree-ring widths, and pollen (Baxter et al., 2023; Chen et al., 2023a, 2023b; Cisneros et al., 2021; Gao et al., 2022; Johnston et al., 2021; Macumber et al., 2018; Peng et al., 2024; Liang et al., 2025; Prentice et al., 2022; Reis et al., 2022; Sha et al., 2023; Xu et al., 2018; Wei et al., 2025). Meanwhile, advancements in tree-ring oxygen isotope analysis have positioned it as a pivotal tool for capturing air and soil moisture signals (Freund et al., 2023; Giguère et al., 2016; Grießinger et al., 2011; Kurita et al., 2016; Li et al., 2019; Rinne et al., 2013; Schollaen et al., 2013; Shekhar et al., 2022; Singh et al., 2019; Xu et al., 2021a, 2021b; Yang et al., 2014; Yue et al., 2024). In the Asian monsoon region, tree-ring  $\delta^{18}\text{O}$  is predominantly controlled by precipitation  $\delta^{18}\text{O}$ , providing valuable insights for reconstructing past precipitation variability (Li et al., 2011a; Pandey et al., 2023; Schollaen et al., 2013; Xu et al., 2015). However, precipitation in this region is influenced by multiple sources, with the East Asian Summer Monsoon (EASM) and South Asian Summer Monsoon (SASM) transporting water vapor from the Pacific and Indian Oceans, respectively, as primary contributors (Deng et al., 2014; Gimeno et al., 2012; Li et al., 2025). As this water vapor moves inland, hydrological processes such as precipitation further modify its isotopic composition (Galewsky et al., 2016; Li et al., 2022). Additionally, local climate variability and westerly disturbances exert significant influence over regional precipitation patterns (Herzschuh et al., 2019; Yao et al., 2008). Consequently, trees and precipitation may derive water from multiple sources (Allen et al., 2019; Gimeno et al., 2012). At the leaf level, processes such as transpiration and moisture stress introduce additional fractionation effects, meaning that the  $\delta^{18}\text{O}$  signal preserved in tree rings reflects a contribution of source water characteristics, local climatic conditions, and large-scale atmospheric circulation patterns (Gessler et al., 2014; Labotka et al., 2016; Li et al., 2011b; Treydte et al., 2014; Vuille et al., 2003). These interacting factors contribute to the complexity of modelling and interpreting tree-ring oxygen isotope records (Loader et al., 2007; Savard and Daux, 2020). Consequently, efforts to detect and attribute the effects of climate change on precipitation variability remain highly challenging.

The advancement of fingerprint modelling has strengthened our ability to utilise climate and hydrological models to detect and attribute past precipitation changes to increasing greenhouse gas (GHG) and aerosol (AERO) emissions (Marvel et al., 2019). The fingerprint is defined as the leading Empirical Orthogonal Function (EOF) of the ensemble mean from the Coupled Model Intercomparison Programme Phase 6 (CMIP6) models for historical and future scenarios spanning 1900 to 2099 (Hasselmann, 1997; Van Vuuren et al., 2011). Given the dominance of GHG and AERO emissions in CMIP6, the fingerprint primarily captures the climate response to anthropogenic forcing (Santer et al., 2011). While fingerprint experiments provide a robust framework for quantifying anthropogenic contributions to precipitation variability, they often rely on relatively short instrumental records for model calibration and validation (Laapple et al., 2023; Hegerl et al., 2019; Roseznig and Neofotis, 2013; Sarojini et al., 2016; Wang et al., 2025). Integrating proxy archives with model data offers an improved climatic context for evaluating long-term precipitation variability, which remains challenging to simulate accurately (Hernández et al., 2020). This method enables models to situate detected anthropogenic changes within a broader temporal framework, extending beyond the instrumental period when human activities exerted their most substantial influence (Bindoff, 2013; Bradley et al., 2003). Furthermore, as tree-ring oxygen isotopes exhibit high sensitivity to moisture transported by atmospheric and oceanic circulation, their climate reconstructions provide deeper insights into internal variability compared to reanalysis

datasets and model simulations (Wernicke et al., 2015; Xu et al., 2023a, 2023b). Such synergistic approaches significantly enhance our understanding of precipitation variability attribution and bolster confidence in detecting the interplay between human activities and natural climate variability.

In this study, we developed a high-resolution annual precipitation reconstruction based on Chinese pine (*Pinus tabulaeformis* Carrière) tree-ring oxygen isotopes to investigate hydroclimatic variability in the NCMMR. We validated our isotope-based reconstruction against other reconstructions derived from different proxy sources. Additionally, we assessed the influence of internal variability and external forcing on past precipitation variations using simulations from the Community Earth System Model-Last Millennium Ensemble (CESM-LME). The internal variability and monsoon index derived from the observational period were employed to validate the attribution results in the CESM-LME simulations. Subsequently, the fingerprint method, based on CMIP6 diagnostic data under historical and SSP585 scenarios, was applied to examine the impact of anthropogenic forcing on precipitation variability.

## 2. Materials and methods

### 2.1. Stable oxygen isotope measurements and chronology development

Tree cores from Chinese pine (*Pinus tabulaeformis* Carrière) were collected (44 cores from 21 trees) from Mount Heng in North China (113°43' E, 39°40' N, 1815 m. a.s.l.; Fig. 1; Table 1; Supporting Information S1). Two cores were extracted from each tree using an incremental drill. The tree-ring samples were fixed in wooden holders, and after the complete drying of white latex, they were sanded with progressively finer sandpaper until the wood cells were clearly visible under a microscope. The width of each tree ring was measured using the CDendro 9.4 analysis system (Cybis Elektronik & Data AB). The COFECHA program was employed for cross-dating to ensure a highly accurate determination of tree age and ring width (Holmes, 1983). The ARSTAN program was applied to generate the ring-width chronology (Cook, 1985).

Among the sampled trees, four older individuals with clearly defined

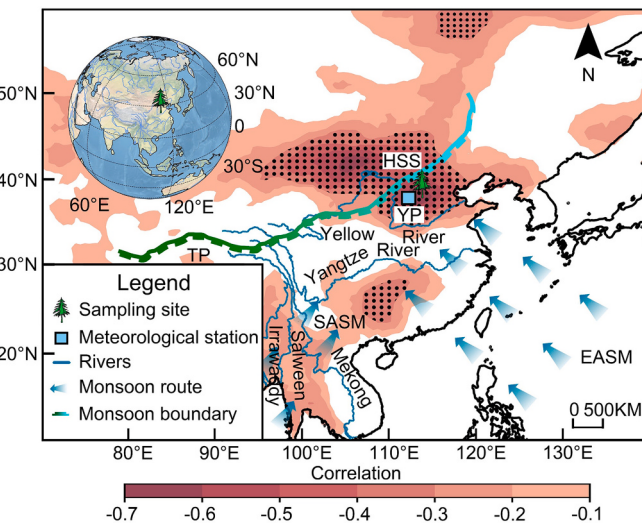


**Fig. 1.** The sampling site (HSS) and meteorological station (Yuanping) were distributed in the North China Monsoon Marginal Region. Spatial correlation based on the composite  $\delta^{18}\text{O}$  chronology and Climatic Research Unit (CRU) TS 4.07 precipitation data (September to August 1955–2020). Black dots indicate 95 % confidence limits for spatial correlation. The monsoon boundary is defined as the 2 mm/day precipitation line in summer (May–September 1955–2020).

**Table 1**The correlation coefficients between the  $\delta^{18}\text{O}$  series and tree ring width series.

	HSS011	HSS032	HSS052	HSS201	HSS index
HSS032	0.47 <sup>a</sup>				
HSS052	0.55 <sup>a</sup>	0.62 <sup>a</sup>			
HSS201	0.71 <sup>a</sup>	0.48 <sup>a</sup>	0.72 <sup>a</sup>		
HSS index	0.78 <sup>a</sup>	0.83 <sup>a</sup>	0.74 <sup>a</sup>	0.90 <sup>a</sup>	
TRW	-0.37 <sup>a</sup>	-0.35 <sup>a</sup>	-0.31 <sup>a</sup>	-0.41 <sup>a</sup>	-0.40 <sup>a</sup>

Note: <sup>a</sup> significant level  $p < 0.001$ , <sup>b</sup> significant level  $p < 0.01$ , <sup>c</sup> significant level  $p < 0.05$ .

rings, designated HSS011 (1776–2020), HSS032 (1770–2014), HSS052 (1774–2020), and HSS201 (1784–2018), were selected for oxygen isotope analysis (Fig. 2a). The  $\alpha$ -cellulose extraction followed an improved plate method, adhering to the chemical treatment procedure outlined in the Jayme-Wise protocol (Schollaen et al., 2017; Xu et al., 2011). The  $\delta^{18}\text{O}$  values were compared with Merck cellulose, with a Merck cellulose sample inserted every eight measurements for calibration (Xu et al., 2015). Oxygen isotope data were reported in  $\delta$  notation, with values expressed per mil (‰) relative to the Vienna Standard Mean Ocean Water (VSMOW). A total of 972 cellulose samples were analysed, with an analytical uncertainty of  $\pm 0.19\text{ ‰}$  ( $n = 116$ ) based on repeated measurements of Merck cellulose. All  $\delta^{18}\text{O}$  series demonstrated strong consistency, with an average range of 30.75 ‰ to 31.35 ‰ and a standard deviation between 1.46 ‰ and 1.66 ‰. The  $\delta^{18}\text{O}$  values were measured using a pyrolysis-type high-temperature conversion elemental analyser (TC/EA, Thermo Scientific) coupled with an isotope ratio mass

spectrometer (Delta V Advantage, Thermo Scientific) at the Key Laboratory of Cenozoic Geology and Environment, Chinese Academy of Sciences, Beijing, China (An et al., 2023). Since these isotopic samples originate from the pith, the linear trend in  $\delta^{18}\text{O}$  was significantly higher during the first half-century of tree growth than in the subsequent two centuries. However, as the baseline window (1770–1819) was expanded, this trend became negligible (Fig. 2b; Supporting Information S1). This suggests the presence of an age-related effect on tree  $\delta^{18}\text{O}$  variations, which declines markedly over time (McCarroll and Loader, 2004). To eliminate the influence of this age-related effect, all  $\delta^{18}\text{O}$  series were detrended. Individual  $\delta^{18}\text{O}$  series were fitted with negative exponential functions, and the composite  $\delta^{18}\text{O}$  chronology was constructed from the detrended data using a double-weighted robust average and normalization to minimise bias from extreme values. The express population signal (EPS) ranged from 0.85 to 0.96, and the inter-series correlation (Rbar) ranged from 0.50 to 0.85 across all periods, confirming the robustness of the chronology and its strong retention of common climatic signals (Fig. 2c). Furthermore, a strong negative correlation was observed between the composite  $\delta^{18}\text{O}$  chronology (HSS) and the tree-ring width (TRW) chronology (standard version), further validating its reliability.

## 2.2. Meteorological and proxy data

Meteorological data were obtained from the Yuanping meteorological station (828 m. a.s.l.), comprising monthly precipitation and temperature records spanning the period from 1954 to 2020 (Fig. 2d, [htt](#)

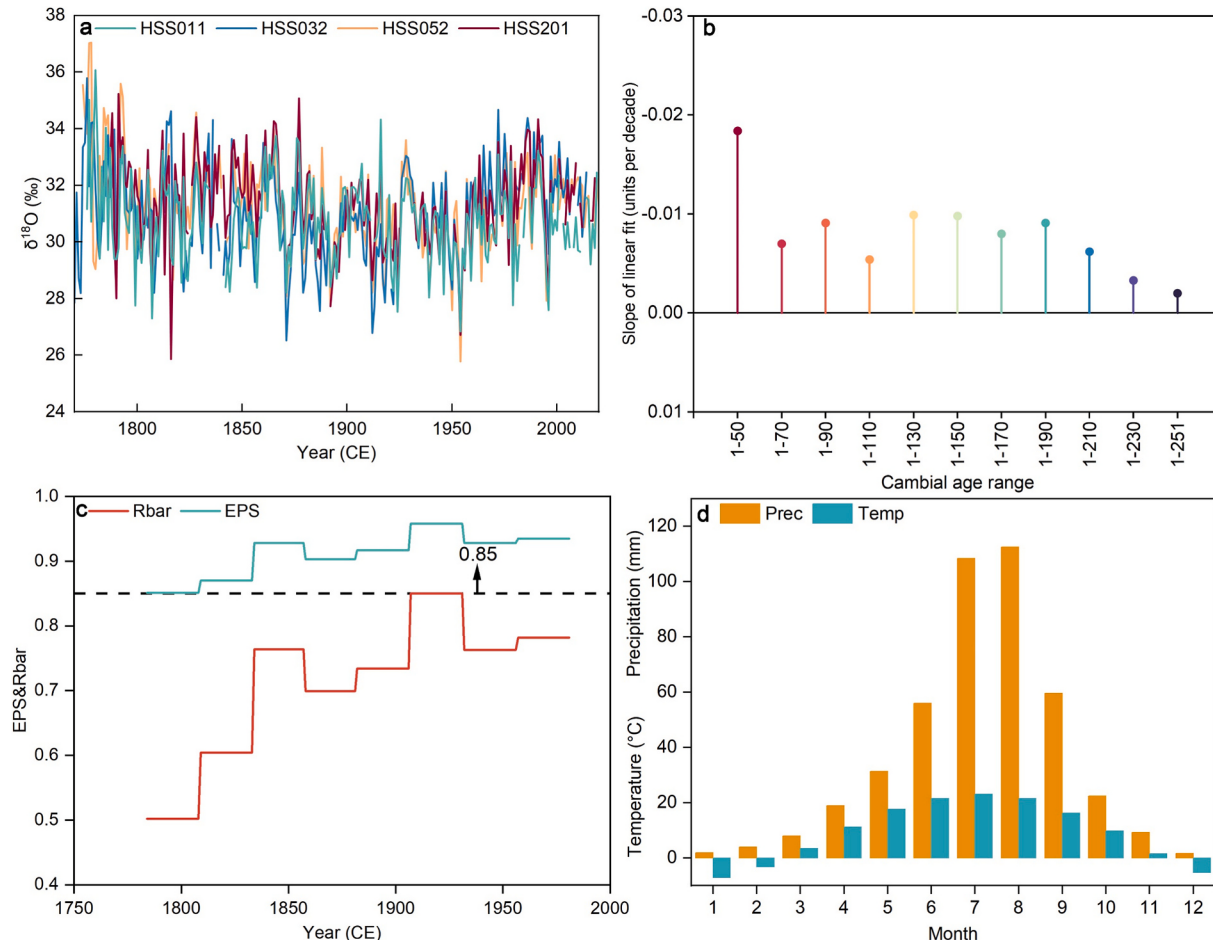


**Fig. 2.** Comparison of changes in HSS011, HSS032, HSS052, HSS201 for  $\delta^{18}\text{O}$  series (a). Based on tree cambial age 1–50 of the linear trend for each 20-year increase in the composite  $\delta^{18}\text{O}$  chronology (b). The composite  $\delta^{18}\text{O}$  chronology EPS and Rbar statistical characteristics (c). Monthly changes in precipitation (Prec) and temperature (Temp) at the Yuanping meteorological station from 1954 to 2020 (d).

<ps://data.cma.cn/>). The spatial correlations between the composite  $\delta^{18}\text{O}$  chronology and climatic factors were assessed using the Climate Explorer provided by the Royal Netherlands Meteorological Institute (KNMI, <https://climexp.knmi.nl/start.cgi>). To investigate the influence of oceanic patterns on climate variability, the Extended Reconstructed Sea Surface Temperature Version 5 (ERSST V5) dataset from the National Oceanic and Atmospheric Administration (NOAA) was utilised, covering the time window from September to August. To examine the teleconnection effects of internal climate variability throughout the observational period (1854–2020), indices of the Atlantic Multidecadal Oscillation (AMO), El Niño–Southern Oscillation (ENSO), Interdecadal Pacific Oscillation (IPO), and Indian Ocean Dipole (IOD) were incorporated, sourced from NOAA (Enfield et al., 2001; Henley et al., 2015; Rayner et al., 2003; Saji and Yamagata, 2003). Additionally, monthly gridded reanalysis datasets for pressure, wind, and humidity from the National Centers for Environmental Prediction (NCEP) were analysed to elucidate the direction and intensity of water vapor transport across North China (September to August). Furthermore, several independent proxy reconstructions have been employed to assess hydroclimatic trends since the mid-20th century (Chen et al., 2020; Cook et al., 2010;

Ge et al., 2016; Hughes et al., 1994; Liu et al., 2019a; Xu et al., 2019; Zhao et al., 2023).

### 2.3. Precipitation reconstruction model

Monthly and seasonal Pearson correlation analyses were conducted to evaluate the relationships between climate variables and the composite  $\delta^{18}\text{O}$  chronology. Given that tree-ring,  $\delta^{18}\text{O}$  exhibits greater sensitivity to precipitation, the strongest correlation was observed within the September–August window (Supporting Information S2). Accordingly, a simple linear regression model was developed to examine the relationship between the composite  $\delta^{18}\text{O}$  chronology and annual precipitation from September of the preceding year to August of the current year (accumulated), covering the period 1955 to 2020 (Fig. 3a).

In the simple linear regression model, the composite  $\delta^{18}\text{O}$  chronology (HSS) was designated as the feature variable ( $X$ ), while precipitation (P9–C8) served as the predictor variable ( $Y$ ). The corresponding regression equations were as follows (Fig. 3b):

$$Y = -2002.2 \times X + 2457.8$$

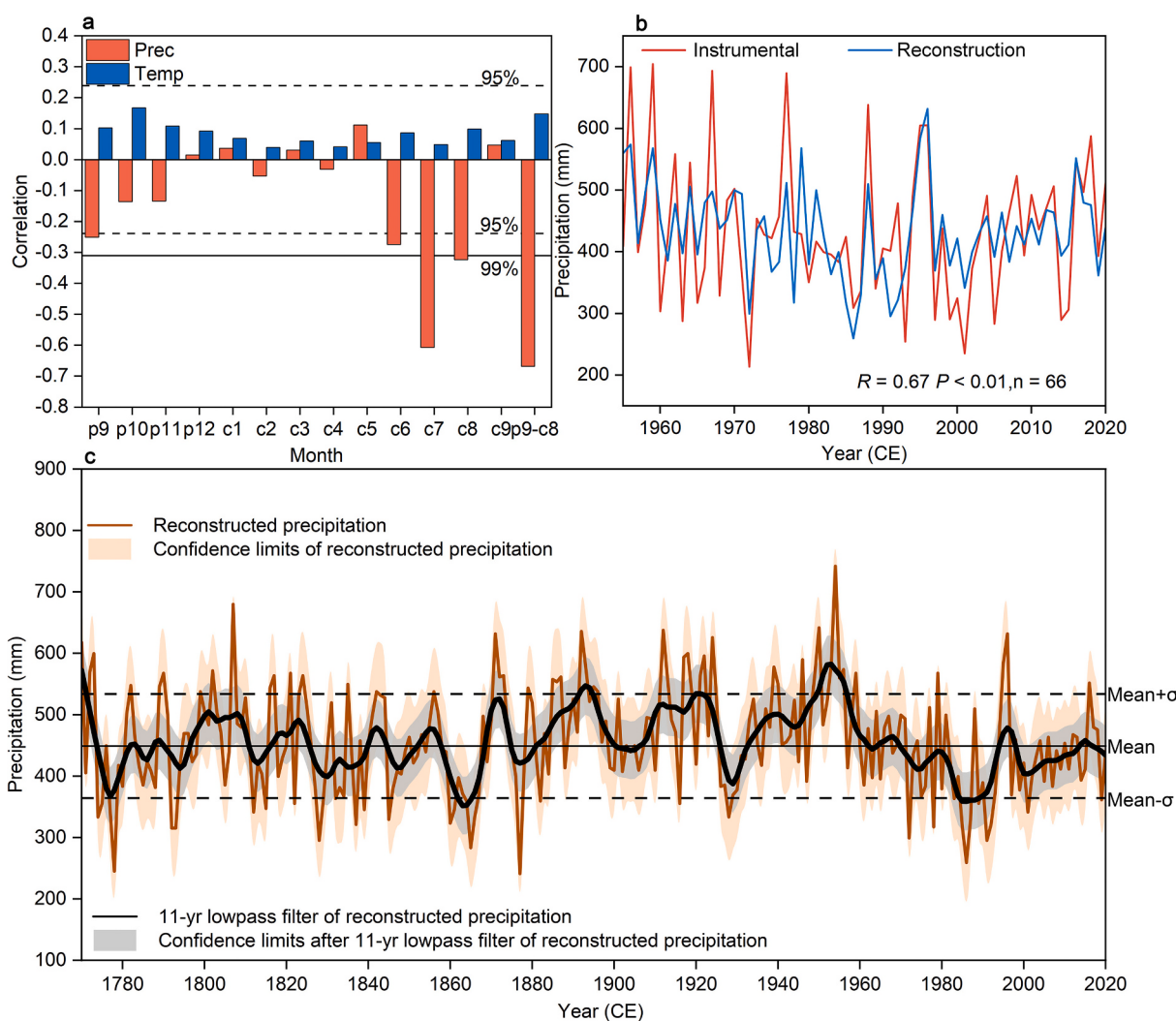


**Fig. 3.** The composite  $\delta^{18}\text{O}$  chronology with instrumental precipitation and temperature (1955–2020) Pearson correlation analysis from September of the previous year to September of the current year (a). ‘p’ represents the previous year and ‘c’ represents the current year. The dashed black line indicates 95 % confidence limit of the reconstructed precipitation and the solid black line indicates 99 % confidence limit of the reconstructed precipitation. The instrumental and reconstructed precipitation comparisons over the modelling period (1955–2020) based on simple linear regression (b). Reconstructed September to August precipitation and 11-year lowpass filter changes for the 1770–2020 (c). Orange shading indicates 90 % confidence limit of reconstructed precipitation. Grey shading indicates 90 % confidence limits after 11-yr lowpass filter of reconstructed precipitation. The dotted line indicates the mean ( $456 \text{ mm}$ )  $\pm$  standard deviation ( $\sigma = 85 \text{ mm}$ ) of the reconstructed precipitation.

Statistical parameters, including the correlation coefficient (R), coefficient of determination ( $R^2$ ), coefficient of efficiency (CE), reduction of error (RE), sign test (ST), and product mean test (PMT), were utilised to evaluate the reliability of the reconstruction model (Supporting Information S2). Extreme event thresholds were defined as one standard deviation ( $\sigma$ ) from the mean. An 11-year low-pass filter was applied to identify long-term trends and transitions between wet and dry periods in precipitation. Cumulative Distribution Functions (CDFs) were employed to analyse the probability distribution of mean precipitation that were not met during the periods 1770–2020 (reconstruction period), 1920–1930 (dry period), and 1950–2020 (dry period).

#### 2.4. Climate model and multiple linear regression

Climate model data were obtained from 13 ensemble members of the CESM-LME (1770–2005), along with simulations from six single-forcing members (Danabasoglu et al., 2020), incorporating land use and land cover (LULC), orbital parameters (ORB), spectral solar irradiance (SSI), volcanic eruptions (VOL), GHG, and AERO (Otto-Btiesner et al., 2016). These simulations offer the most comprehensive representation of historical anthropogenic and natural forcing factors (Collins et al., 2017). The IPO, IOD, and AMO indices (1770–2005) were extracted from sea surface temperature (SST) simulations across all ensemble members of the CESM-LME full-forcing experiment. However, it should be noted that the multi-member mean may not fully capture internal variability. The IPO index was derived from the difference between the SST averaged over the central equatorial Pacific ( $10^\circ\text{S}$ – $10^\circ\text{N}$ ,  $170^\circ\text{E}$ – $90^\circ\text{W}$ ) and the mean SST in the Northwest ( $25^\circ\text{N}$ – $45^\circ\text{N}$ ,  $140^\circ\text{E}$ – $145^\circ\text{W}$ ) and Southwest Pacific ( $50^\circ\text{S}$ – $15^\circ\text{S}$ ,  $150^\circ\text{E}$ – $160^\circ\text{W}$ ) (Henley et al., 2015). The IOD index was calculated as the difference in mean SST anomalies between the tropical western Indian Ocean ( $50^\circ\text{E}$ – $70^\circ\text{E}$ ,  $10^\circ\text{S}$ – $10^\circ\text{N}$ ) and the equatorial southeastern Indian Ocean ( $90^\circ\text{E}$ – $110^\circ\text{E}$ ,  $10^\circ\text{S}$ – $0^\circ$ ) (Saji et al., 1999). The AMO index was obtained by computing the area-averaged sea surface temperature anomalies in the North Atlantic ( $0$ – $70^\circ\text{N}$ ) after detrending and applying a low-pass filter (Schlesinger and Ramankutty, 1994; Kerr, 2000). Zonal wind (U), meridional wind (V), and specific humidity (Q) were extracted from the CESM-LME full-forcing simulation to calculate water vapor transport anomalies for the period 1770–2005. Additionally, the EASM index was derived from the Twentieth Century Reanalysis v3 datasets based on the monsoon index definition of Guo (1983), while the SASM index was reconstructed following Shi et al. (2014). To mitigate the influence of strong long-term trends, all datasets (including internal variability and climate factors) were detrended using least squares regression.

The single-forcing and internal variability factors were standardised, and additional noise was removed by applying filters. Insignificant individual factors were discarded before rerunning the model to derive the multiple linear regression (MLR) equation. The MLR equations for the full-forcing experiment using CESM-LME data are as follows:

$$\begin{aligned} \text{Pre}_{\text{sim}} = & \beta_0 + \beta_1 \text{Pre}_{\text{LULC}} + \beta_2 \text{Pre}_{\text{ORB}} + \beta_3 \text{Pre}_{\text{SSI}} + \beta_4 \text{Pre}_{\text{VOL}} + \beta_5 \text{Pre}_{\text{GHG}} \\ & + \beta_6 \text{ACF}_{\text{IPO}} + \beta_7 \text{ACF}_{\text{AMO}} + \beta_8 \text{ACF}_{\text{IOD}} \end{aligned}$$

Here,  $\text{Pre}_{\text{sim}}$  represents the simulated precipitation predicted by all variables,  $\beta_i$  represents the scale factor for all variable, while  $\text{Pre}_i$  and  $\text{ACF}_j$  denote the precipitation simulated by single-forcing factors and internal variability, respectively. The explained variance, reflecting the relative contribution of all variables in the simulation experiment, was computed as follows:

$$\text{EXP}_i = \frac{|\beta_i| R^2}{\sum_{i=1}^n |\beta_i|} \times 100\%$$

where  $\text{EXP}_i$  represents the explained variance of individual variables,  $\beta_i$  denotes the scaling factor, and  $R^2$  corresponds to the total explained

variance of the MLR.

#### 2.5. Detection and attribution for fingerprint

##### 2.5.1. Description of the fingerprint method

The fingerprint method was employed to identify anthropogenic impacts on climate change in the NCMMR. The fingerprint is defined as the first leading EOF of the spatiotemporal vector covariance matrix (Hasselmann, 1997). Prior to ensemble averaging, the matrix was computed for each CMIP6 model member, ensuring that no single member disproportionately influenced the ensemble mean (Supporting Information S4). Given that internal variability is uncorrelated between the ensemble model and individual members, the leading EOF serves as an indicator of both natural and anthropogenic external forcings (Santer et al., 2013).

##### 2.5.2. CMIP6 diagnostic process

As historical simulations within CMIP6 concluded in 2015, projections were extended to 2100 based on the SSP585 scenario (Supporting Information S4). The SSP585 scenario, in which GHG forcing is the predominant driver, is considered representative of climate response to anthropogenic GHG emissions (Madakumbura et al., 2021; Roesch et al., 2024). Ensemble empirical model decomposition (EEMD) was applied to all CMIP6 members to extract non-linear trends, and the climate model was calibrated using Climatic Research Unit (CRU) TS 4.07 precipitation data. The dataset was subsequently downscaled to a  $0.5^\circ \times 0.5^\circ$  grid using bilinear interpolation (Harris et al., 2020; Xu et al., 2021a, 2021b). The multi-model ensemble (MME) mean summer (June–August, JJA) precipitation was derived for the grid ( $36^\circ\text{N}$ – $39^\circ\text{N}$ ,  $113^\circ\text{E}$ – $117^\circ\text{E}$ ) across all ensemble members from both historical simulations and the SSP585 scenario. The fingerprint was defined as the first leading EOF of the MME mean precipitation from 1850 to 2100, computed with grid-weighted averaging (Supporting Information S4).

##### 2.5.3. Signal and noise

The fingerprint is a function of the latitude (x) and longitude (y) within the spatial domain  $F(x, y)$ . For observed or modelled data  $M(x, y, t)$ , the projection  $R(t)$  of the fingerprint is expressed as follows:

$$R(t) = \sum_{x,y} F(x, y) M(x, y, t) S(x, y)$$

where  $S(x, y)$  represents the grid region. If the identified fingerprint is present in the data,  $R(t)$  exhibits an increasing trend. The signal (S) is defined as the long-term trend in  $R(t)$ , determined using least squares regression (Santer et al., 2011).

To project internal variability onto the fingerprint, precipitation data from Shi et al. (2017) were first projected onto the fingerprint derived from the model, using precipitation values prior to 1850 to represent pre-industrial noise resulting from natural forcing or internal variability. Secondly, precipitation was calculated for all variables in the CMIP6 pre-industrial control simulations. By linking each pre-industrial control simulation for precipitation and projecting the results onto the corresponding fingerprint, a long predictive time series (1770–2100) was obtained (Marvel et al., 2019). All possible trend lengths were computed at 50-year intervals within this series. The standard deviation of this distribution provided a measure of noise (N) in the trends, indicating the likelihood that observed signals were attributable to internal variability. The signal-to-noise ratio (S/N) was standardised, and a two-tailed Z-test was employed to estimate significance levels. An S/N exceeding 0.95, 1.64, or 2.57 corresponded to confidence levels of 66 %, 90 %, and 99 %, respectively, categorised as *likely*, *very likely*, and *almost certain* in the mean signal (Bindoff, 2013). The time at which the GHG forcing signal is expected to emerge from natural climate variability is defined as the point when the average signal in the model exceeds the reconstructed pre-industrial variability.

### 3. Results

#### 3.1. Climatic sensitivity of tree-ring stable oxygen isotopes

Tree growth is influenced by the lagged effects of moisture conditions from the preceding year (Littell et al., 2008; Huang et al., 2010; Hacket-Pain et al., 2018; Babst et al., 2019; Hammond et al., 2022). Although lag effects do not directly govern tree growth in the current year, they are undeniably linked to tree physiological processes (Supporting Information S2) (Babst et al., 2013). Dendrochronological research in northern China has demonstrated the presence of hydroclimatic lag effects on tree growth (Yang et al., 2020). Instrumental precipitation records from September to August exhibit a strong correlation with the composite  $\delta^{18}\text{O}$  chronology (HSS), reflecting variations in annual moisture availability and monsoon intensity ( $R = -0.67$ ; Fig. 3a, b; Supporting Information S2). Previous studies have shown that precipitation in the NCMMR is particularly sensitive to variations in the strength of the ASM (Liu et al., 2019b). The ASM influenced May–September (368 mm) precipitation accounts for ~85 % of the total annual (434 mm) precipitation (1955–2020) in the NCMMR (Fig. 2d). Therefore, the composite  $\delta^{18}\text{O}$  chronology was utilised to reconstruct precipitation changes from September to August over the period 1770–2020 in the NCMMR (Fig. 3c).

#### 3.2. Reconstructed precipitation changes

The reconstructed precipitation record underwent rigorous cross-validation tests, explaining ~40 % and ~51 % of the variance for the periods 1955–1988 and 1989–2020, respectively (Table 2). The model exhibited robustness across the full calibration period, explaining ~45 % of the variance from 1955 to 2020 (Table 2). During model validation, the reconstructed precipitation closely matched instrumental data (Fig. 3b). The model successfully passed the RE and CE tests, indicating that the reconstructed precipitation series is reasonably reliable (Table 2). The sign test further confirmed that the model was consistent with instrumental data in capturing low-frequency variations (Table 2). The PMT yielded a value of 6.38, suggesting minimal differences between instrumental and reconstructed precipitation records (Table 2). Therefore, the reconstructed precipitation from September of the previous year to August of the current year can be considered reliable. Additionally, autocorrelation was not a significant factor in the composite  $\delta^{18}\text{O}$  chronology, as indicated by a Durbin-Watson statistic of 2.01.

Over the past 251 years, the NCMMR has experienced distinct dry and wet periods, with a mean precipitation value of 456 mm. Prolonged dry periods were observed during 1774–1788, 1826–1840, 1858–1868, 1970–1994, and 1998–2014, while wet periods occurred in 1797–1810, 1883–1899, 1908–1925, and 1934–1961 (Fig. 3c). Extreme wet years, defined as those exceeding one standard deviation (85 mm) above the historical mean, occurred 44 times, whereas extreme dry years were recorded 39 times (Fig. 3c; Supporting Information S2). Moreover, our reconstruction captured large-scale precipitation variability, which is strongly influenced by ASM dynamics (Fig. 1). In the NCMMR, the ASM governs both the total precipitation and the  $\delta^{18}\text{O}$  signature of precipitation water during the growing season (Fan et al., 2022). This suggests that precipitation water is imprinted by “large-scale” remote

phenomena that transport humidity to the NCMMR (Dansgaard, 1964; Li et al., 2023; McCarroll and Loader, 2004; Wang et al., 2020b). Further comparisons revealed that hydroclimatic archives from the South Asian and East Asian monsoon regions recorded similar drying events since the 1900s (Fig. 4). Specifically, a downward trend has been observed in the oxygen isotope record of the Ordos Plateau ( $R = -0.52$ ,  $P < 0.01$ ,  $n = 205$ ) and the Yellow River runoff reconstruction ( $R = 0.25$ ,  $P < 0.01$ ,  $n = 243$ ), both of which were significantly correlated with the reconstructed precipitation (Fig. 4; Supporting Information S2). A similar downward trend was also identified in the Chao Phraya River peak season flow records ( $R = 0.06$ ,  $P > 0.05$ ,  $n = 202$ ) and the Palmer Drought Severity Index (PDSI) reconstruction ( $R = 0.10$ ,  $P > 0.05$ ,  $n = 236$ ) derived from the Monsoon Asia Drought Atlas (MADA). However, these records were not significantly correlated with the reconstructed precipitation (Fig. 4). These findings suggest that the decline in monsoon precipitation (~14 mm per decade, 1950–2020) is neither a purely regional nor an isolated phenomenon. Instead, the widespread drying trend reflects common hydroclimatic patterns and shared forcing mechanisms.

#### 3.3. Long-term effects of atmosphere-ocean circulation on precipitation variability

The relationship between reconstructed precipitation and global SSTs revealed significant anomalies in the Pacific, Indian, and Atlantic Oceans (Fig. 5a, b). These anomalies were further reflected in the significant correlations between reconstructed precipitation and the IOD ( $R = -0.26$ ,  $P < 0.01$ ,  $n = 151$ ), IPO ( $R = -0.28$ ,  $P < 0.01$ ,  $n = 167$ ; after 11-year low-pass filtering,  $R = -0.29$ ,  $P < 0.01$ ), and ENSO ( $R = -0.36$ ,  $P < 0.01$ ,  $n = 151$ ) indices. However, no significant correlation was observed with the AMO ( $R = -0.02$ ,  $P > 0.05$ ,  $n = 165$ , after 11-year low-pass filtering,  $R = -0.05$ ,  $P > 0.05$ ) (Fig. 5c, d, e, f). Nonetheless, running correlation analyses using a 30-year window indicated that the relationship between AMO and precipitation strengthened after the mid-20th century (Supporting Information S3). Due to the length limitations of reanalysis data, it was not possible to comprehensively assess the long-term link between precipitation and atmosphere-ocean patterns. Therefore, simulated precipitation and SST data from the CESM-LME were utilised to validate this relationship over an extended timescale.

The MLR modelling was conducted to quantify the contribution of internal variability, incorporating forced experiments from CESM-LME (1770–2005). External forcing factors were included for comparison; however, ENSO was excluded due to its covariance with IPO. Internal variability and external forcing collectively explained ~67 % of simulated precipitation variability (Fig. 6a). Among internal variability factors, the IOD accounted for ~30 % of the variance, while the AMO and IPO contributed ~11 % and ~10 %, respectively (1770–2005). In contrast, external forcing factors, including GHG, LULC, ORB, SSI, and VOL, explained ~1 %, ~5 %, ~3 %, ~6 %, and ~1 % of the variance, respectively (Fig. 6a). When assessed within a consecutive 50-year window, the variance in simulated precipitation explained by internal variability exhibited temporal fluctuations (Supporting Information S3). Water vapor transport analyses in CESM-LME further indicated that different phases of the IOD, IPO, and AMO exerted strong influences on simulated precipitation since 1770 (Fig. 6b, c, d, e, f, g; Supporting Information S3). Therefore, CESM-LME simulated precipitation can serve

**Table 2**

Statistical characteristics of simple linear regression model for reconstructed precipitation.

Calibration	R	R <sup>2</sup>	DW	Verification	R	R <sup>2</sup>	ST	PMT	RE	CE	DW
1955–1988	0.63 <sup>a</sup>	0.40 <sup>a</sup>	2.27	1989–2020	0.72 <sup>a</sup>	0.51 <sup>a</sup>	27+/5- <sup>a</sup>	4.02	0.51	0.50	1.56
1989–2020	0.72 <sup>a</sup>	0.51 <sup>a</sup>	1.58	1955–1988	0.63 <sup>a</sup>	0.40 <sup>a</sup>	25+/9- <sup>a</sup>	4.95	0.40	0.39	1.70
1955–2020	0.67 <sup>a</sup>	0.45 <sup>a</sup>	2.01				51+/15- <sup>a</sup>	6.38	0.44	0.45	

Note: R = correlation coefficient,  $R^2$  = explained variance, ST = sign test, PMT = product mean test, RE = reduction of error, CE = coefficient effective, DW = Durbin-Watson test, <sup>a</sup> significant level  $p < 0.01$ , <sup>b</sup> significant level  $p < 0.05$ .

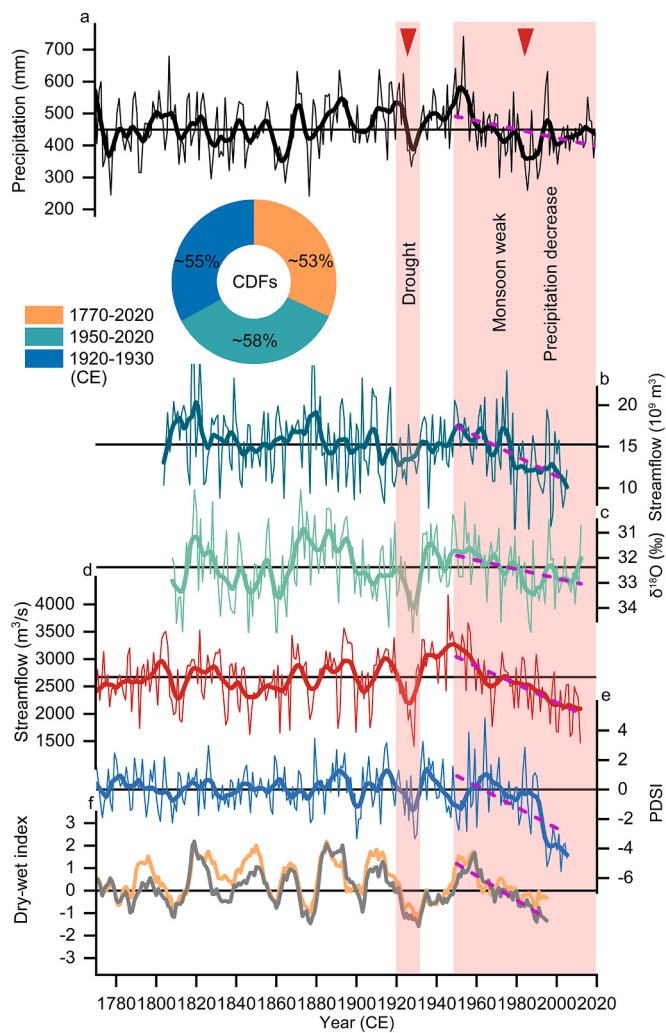


**Fig. 4.** Comparison of hydroclimatic records include the precipitation reconstruction for this study from 1770 to 2020 (a), Chao Phraya River peak season flow variation based on the tree ring  $\delta^{18}\text{O}$  from 1804 to 2005 (b; Xu et al., 2019), Ordos Plateau tree ring  $\delta^{18}\text{O}$  values from 1808 to 2012 (c; Liu et al., 2019a), middle Yellow River streamflow reconstruction based on the tree ring width from 1770 to 2012 (d; Chen et al., 2020), Monsoon Asia Drought Atlas for summer PDSI reconstruction based on the tree rings, and the PDSI grid selected range is 36°N–39°N, 113°E–117°E, and the years selected is 1770–2005 (e; Cook et al., 2010), Regional dry-wet index series for northern China (gray) and eastern central (yellow) China based on the multisource proxy records from 1770 to 1995 (f; Ge et al., 2016). The  $\delta^{18}\text{O}$  record and reconstructed precipitation have opposite y-axes. Red shading indicates the common decline period of all series reported in our reconstruction. Cumulative Distribution Functions (CDFs) probability of not satisfying the long-term mean (456 mm, 1770–2020) of precipitation reconstruction in three period (1770–2020, 1950–2020, 1920–1930). The purple dotted line indicates the linear trend since 1950 of Fig. 4a-f. (For interpretation of the references to colour in this figure legend, the reader is referred to the web version of this article.)

as a representative proxy for  $\delta^{18}\text{O}$ -based precipitation reconstructions over longer timescales to identify the source of the driving factor, despite being primarily dominated by internal variability (Fig. 7). Moreover, we found that the EASM and SASM were not only strongly correlated ( $P < 0.05$ ) with both simulated and reconstructed precipitation, but were also direct linked ( $P < 0.05$ ) to internal variability factors (Supporting Information S3).

### 3.4. Anthropogenic forcing detected by the fingerprint

The MLR results highlighted the dominant role of internal variability in precipitation changes at the NCMMR based on CESM-LME simulations (1770–2005). However, the effect of external forcing (both anthropogenic and natural) was not statistically significant (Fig. 6a; Supporting Information S3). This discrepancy may be attributed to the strong sensitivity of modelled precipitation to internal variability (Otto-Blienes et al., 2016). Therefore, the fingerprint method was applied to further assess the extent of climate change driven by anthropogenic factors (Bonfils et al., 2020; Madakumbura et al., 2021; Roesch et al., 2024). The results indicate that the GHG forcing (signal emerged) strongly influenced precipitation changes in the 1950s (*very likely*, 90 % confidence), and that this effect diminished rapidly between the 1970s and 1990s (Fig. 8). The GHG signal re-emerged since 2008 (*very likely*, 90 % confidence) and almost certainly (99 % confidence) became a dominant contributor to the precipitation trend in the next few decades (Fig. 8). Although precipitation changes are strongly associated with forcing factors in the fingerprint, potential biases may arise due to model accuracy constraints.

It is important to note that, unlike CESM-LME simulations (forcing experiments), the fingerprint method accounts for the influence of natural forcings, such as volcanic activity and solar radiation, had no statistically significant effect on precipitation variability in the NCMMR during the pre-industrial period, meaning that the fingerprint mainly reflects the extent of internal variability (Supporting Information S4). For post-industrial precipitation changes, the expansion of internal variability (predominance impact on precipitation) observed in the pre-industrial period can be disentangled from anthropogenic forcing, which is primarily dominated by GHG emissions in CMIP6 simulations (historical and SSP585 scenarios) for the period 1950–2100 (Marvel et al., 2019). Consequently, fingerprints provide a means of detecting precipitation changes influenced by post-industrial GHG forcing or human activities.

## 4. Discussion

### 4.1. Widespread precipitation decrease since the mid-20th century

A new precipitation reconstruction for the NCMMR was developed based on  $\delta^{18}\text{O}$  data, covering the period 1770–2020. The reconstructed precipitation closely aligns with instrumental records over the modelling period, demonstrating its reliability as an indicator of ASM intensity in the monsoon marginal region (Fig. 3b; Table 2; Supporting Information S3) (Liu et al., 2019b). Although variations in elevation and climatic conditions exist across East Asia, the reconstructed precipitation series exhibits strong correlations and similar trends with independent hydroclimatic records (Fig. 4). This relationship suggests that the reconstructed dataset effectively represents long-term moisture variations over extensive spatial domains and serves as a robust and reliable proxy record. Additionally, the reconstruction successfully captures extreme events documented in historical records. Notable examples include the North China famine of 1876–1878 (Dingwu Famine, 352 mm,  $-1.2\sigma$ ), the severe drought in East Asia from 1999 to 2001 (380 mm,  $-0.9\sigma$ ), which led to reduced food production and significant economic losses, and the heavy rainfall event of 2016 (552 mm,  $+1.1\sigma$ ), which resulted in severe flooding in the Yellow River Basin (Deng, 2020; Liang et al., 2006; Wang et al., 2017; Wu et al., 2011; Zhao et al., 2023).

The reconstructed precipitation record further highlights a persistent decline in precipitation ( $-1.4$  mm per year) since the 1950s, with values (445 mm,  $-0.1\sigma$ , 1950–2020) significantly below the long-term mean (Fig. 3c). Recent studies suggest that this drying trend has been unprecedented in ASM-dominated regions over the past four centuries (Cai et al., 2022; Kumar et al., 2020; Liu et al., 2019b; Ueda et al., 2006). Hydroclimatic and isotope records along the EASM and SASM pathways

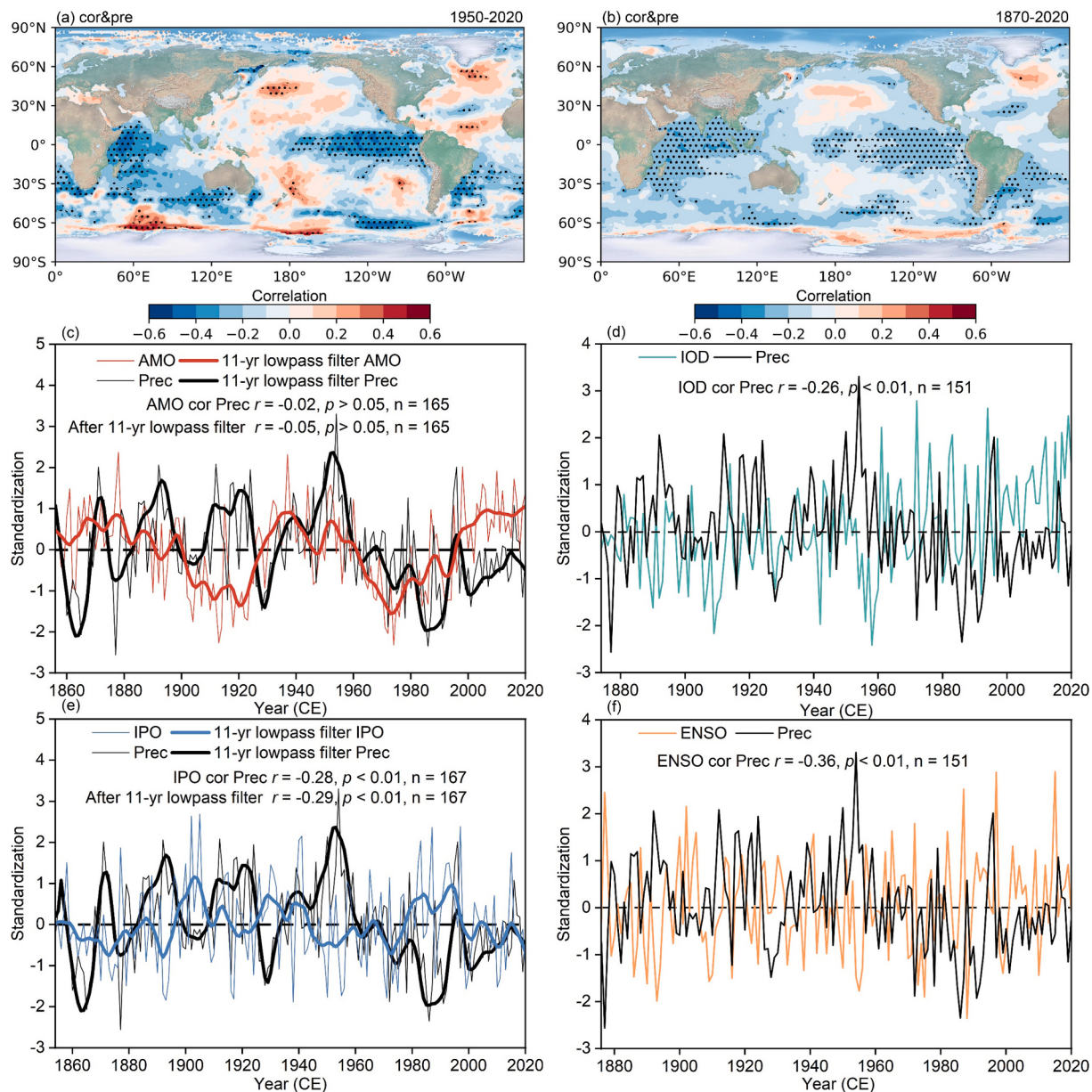


**Fig. 5.** The 1950–2020 (a) and 1870–2020 (b) spatially correlation (September–August) for reconstructed precipitation and sea surface temperature (SST). Black dots indicate the 95 % confidence limits for spatial correlation. Cor&pre represents the spatial correlation between reconstructed precipitation and SST. The comparisons of reconstructed precipitation and calculated AMO (1856–2020) (c), IOD (1870–2020) (d), IPO (1854–2020) (e), and ENSO (1870–2020) (f) indices from the National Oceanic and Atmospheric Administration (NOAA). Thin lines indicate raw values, thick lines indicate 11-yr lowpass filter.

have also supported this drying trend since the 1950s (Fig. 4). However, the precipitation decline observed in the  $\delta^{18}\text{O}$  record appears comparatively weaker, possibly reflecting regional variations in the magnitude and intensity of moisture reductions (Supporting Information S2).

#### 4.2. Response of precipitation to the coupled atmosphere-ocean system in the North China Monsoon Marginal Region

Weakened water vapor transport increases the likelihood of drought in monsoon-dominated regions of East Asia (Battipaglia et al., 2008; Labuhn et al., 2014). Previous studies have demonstrated that variations in monsoon intensity, driven by SST anomalies in the Pacific and Indian Oceans, as well as shifts in the position of the subtropical high-pressure system, influence water vapor transport to North China (Han et al., 2018; Qu et al., 2024; Zhou and Yu, 2005). Meanwhile, the Atlantic Ocean modulates the water vapor supply to North China via the

westerlies and the ASM system, likely through teleconnection effects on circulation patterns over the Eurasian continent (Chen et al., 2023a, 2023b; Li et al., 2024). Our findings underscore the relationship between reconstructed precipitation and global SST anomalies, suggesting that oceanic patterns play a key role in regulating water vapor transport mechanisms and contributing to regional droughts (Fig. 5; Supporting Information S3). This conclusion aligns with previous hydroclimatic studies conducted on the Loess Plateau (Liu et al., 2022; Cao et al., 2025).

The results from CESM-LME simulations and fingerprint analysis indicate that precipitation variability and water vapor transport in the NCMMR were primarily driven by internal variability until the 1950s. External forcing factors, including VOL, LULC, and ORB, exerted relatively weak influences until the emergence of the anthropogenic GHG signal in the mid-20th century (Figs. 6, 8; Supporting Information S3, S4). Although the contributions of different internal variability factors,

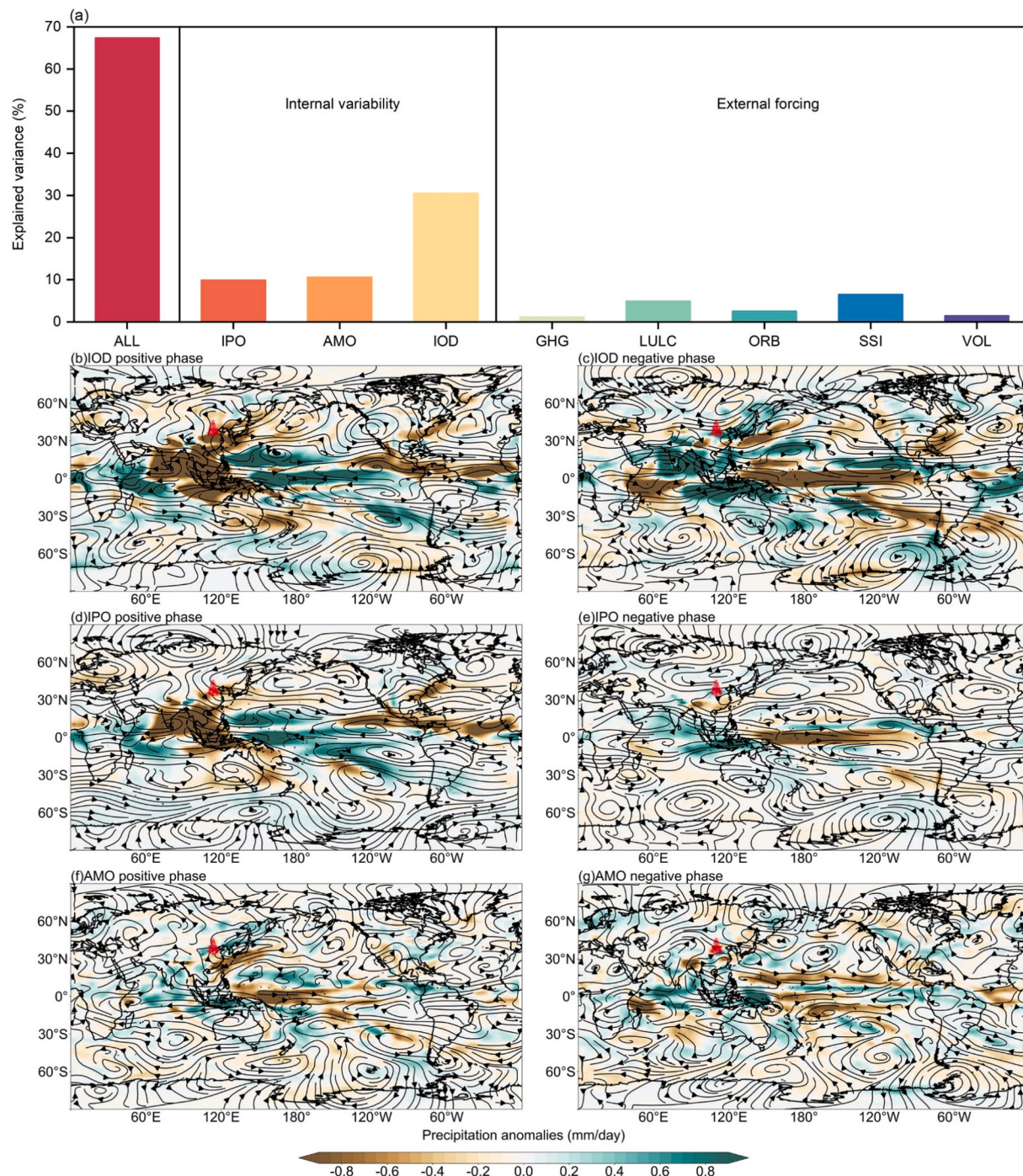


**Fig. 6.** The explained variance (For calculation, see Materials and Methods for climate model and multiple linear regression (a). Composite of simulated precipitation and 500 hPa water vapor transport anomalies (vectors, where  $uq$  and  $vq$  are multiplied by 1000) for IOD (b, c), IPO (d, e), and AMO (f, g) in the positive and negative phases, and simulated precipitation and water vapor data were obtained from the CESM-LME simulations (For calculation, see Materials and Methods for climate model and multiple linear regression). Positive or negative phases were selected as combinations of years 1770–2005 when the IOD, IPO, and AMO were above or below standard deviation from the CESM-LME simulations. Red trees indicate study sites. (For interpretation of the references to colour in this figure legend, the reader is referred to the web version of this article.)

such as the IPO, AMO, and IOD, to precipitation changes have varied over time, internal variability has remained the dominant driver of precipitation trends (Supporting Information S3) (Han et al., 2023). Multi-proxy records from the East Asian monsoon region similarly highlight the deterministic role of internal variability in historical hydroclimatic changes (Hu et al., 2023). Notably, due to strong interactions among internal variability factors, these oscillations influence

the ASM system and, consequently, regulate water vapor transport to monsoon regions (Supporting Information S3) (Dong et al., 2024; Kang and Yang, 2015; Song et al., 2020; Xiao et al., 2015; Zhang et al., 2022a). For instance, the influence of ENSO on precipitation variability in the EASM region may be modulated by the IPO, with the ENSO-EASM relationship being stronger during the positive phase of the IPO than during its negative phase (Zhang et al., 2022b). The strong correlation

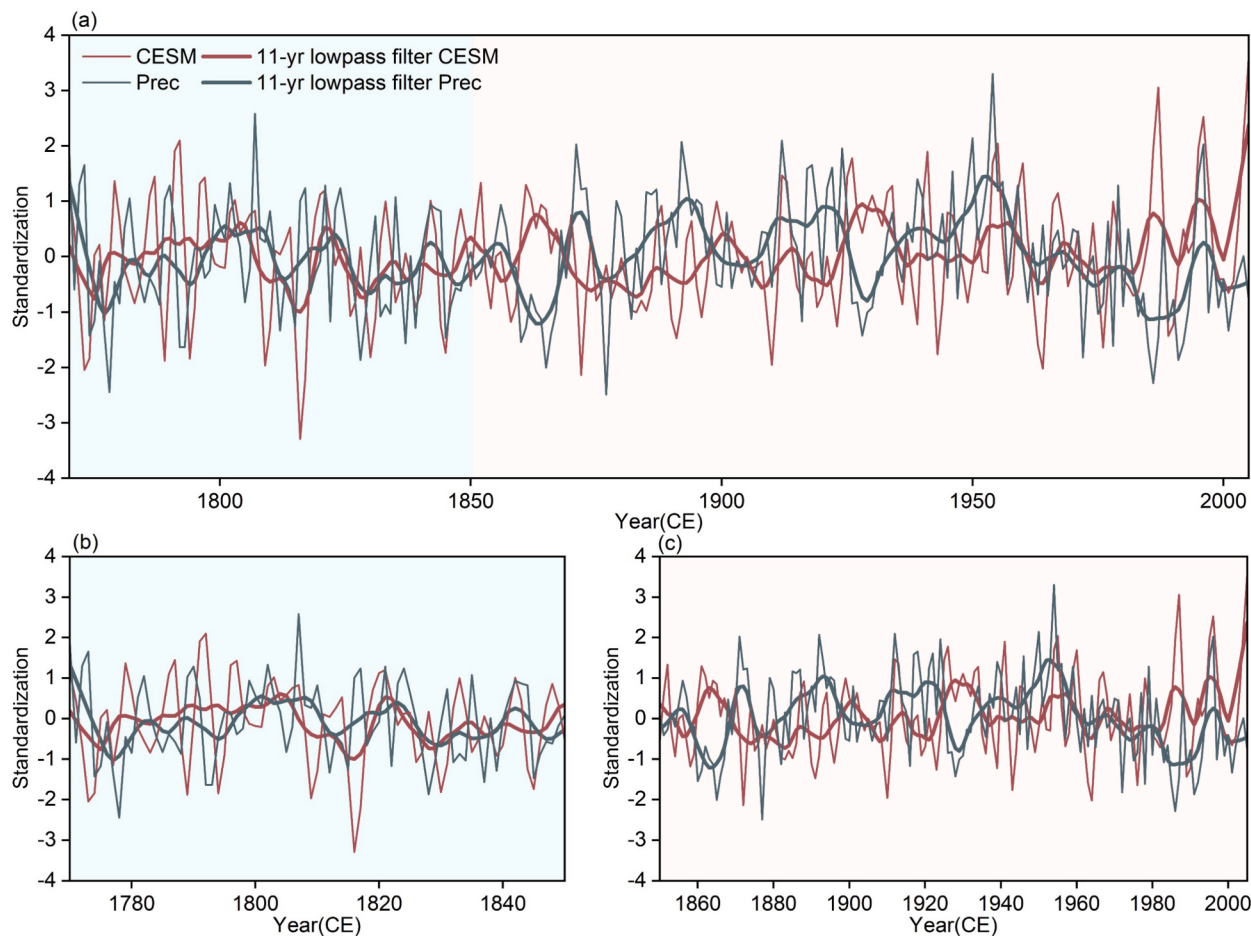


**Fig. 7.** CESM-LME simulated precipitation based on the multiple linear regression and reconstructed precipitation are compared over 1770–2005 (a), 1770–1850 (b), and 1851–2005 (c). Thin lines indicate raw values, thick lines indicate 11-yr lowpass filter. The correlation coefficients were calculated based on 11-yr of lowpass filter.

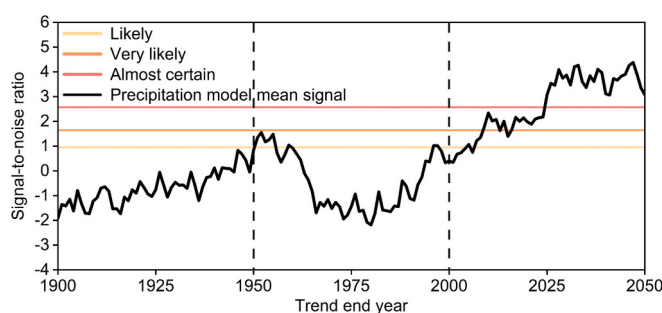


**Fig. 8.** Time of forcing signals based on the precipitation model fingerprint method. Black line indicates the multi-model ensemble signal-to-noise ratio (For calculation, see Materials and Methods for detection and attribution for fingerprint). Vertical dash lines indicate the years 1950 and 2000.

between EASM and SASM and internal variability supports the hypothesis that atmosphere-ocean interactions regulate monsoon precipitation by influencing the ASM system (Supporting Information S3).

The persistent drying trend observed in the NCMMR since the mid-20th century can be attributed to the phase transitions of internal variability factors. This relationship was confirmed by the strong influence of water vapor transport on precipitation during different phases of the IPO, AMO, IOD, and ENSO, as evidenced by analyses of NCEP reanalysis data and CESM-LME simulations. Specifically, the positive phase of the IOD weakens precipitation transport from south-westerly

winds to North China, while increasing SSTs in the Indian Ocean alter the ocean-land thermal gradient in East Asia, thereby weakening both the SASM and the EASM water vapor (Fig. 6b, c; Supporting Information S3) (Qiu et al., 2014; Schott et al., 2009). The positive phase of the IPO reduces Walker Circulation intensity, suppresses convection over the Indo-Pacific Warm Pool, weakens ASM activity, strengthens subtropical high pressure over the western Pacific, and diminishes water vapor transport to North China (Fig. 6d, e; Supporting Information S3) (Aihaiti et al., 2023; Wyatt, 2020; Xu et al., 2023a, 2023b). During the negative phase of the AMO, the wave train propagating from the Atlantic Ocean to the North Pacific is weakened, leading to reduced long-distance water vapor transport and diminished ASM activity, ultimately contributing to decreased precipitation in North China (Fig. 6f, g; Supporting Information S3) (Bollasina and Messori, 2018; Si et al., 2021; Yu et al., 2024). Additionally, the ENSO index (Nino 3.4) and reconstructed precipitation exhibit a significant negative correlation, indicating the regulatory role of ENSO in North China precipitation at the interannual scale (Fig. 5f, Supporting Information S3) (Cai et al., 2015; Collins and The, 2005; Li et al., 2020). Notably, the ability of CESM-LME simulations to accurately capture water vapor sources may be weaker compared to NCEP reanalysis data. To improve the reliability of our findings, multiple validations were conducted using NCEP reanalysis data and reconstructed precipitation (Supporting Information S3). This validation process benefited from the strong sensitivity of  $\delta^{18}\text{O}$  to atmospheric and soil moisture conditions.

#### 4.3. Anthropogenic forcing strongly influences precipitation variability in the North China Monsoon Marginal Region

Attributing climate change to external forcing or internal variability has become increasingly complex, especially when integrating multiple climate models (Bathiany et al., 2016; Bonfils et al., 2020; Chen et al., 2021; Raihani and Aitken, 2011; Stott et al., 2004). In the NCMMR, GHG forcing may have briefly affected precipitation in the 1950s, reaching a 90 % confidence level, but this effect subsequently weakened and became undetectable during the latter half of the 20th century (Fig. 8). This suggests that the elevated precipitation observed in the 1950s was initially driven by GHG forcing, aligning with global trends of anthropogenically induced precipitation intensification over land (Banerjee and Singh, 2022; Paik et al., 2020; Risser et al., 2024; Zhou et al., 2023). However, the decline in precipitation observed during the 1970s was likely attributable to increased AERO concentrations, which counteracted the warming effect of GHG forcing. Previous studies have demonstrated that aerosol-induced cooling can trigger droughts, whereas increased GHG emissions may promote regional wetting (Palmer et al., 2023; Zhao et al., 2024). Evidence from CESM-LME simulations supports this attribution (Fig. 7). The strong positive correlation between CESM-LME-simulated and reconstructed precipitation before the Industrial Revolution ( $R = 0.54$ ,  $P < 0.01$ , 1770–1850) became a significant negative correlation after incorporating AERO experiments in the post-industrial period ( $R = -0.30$ ,  $P < 0.01$ , 1851–2005). Besides the phase shift impact of the internal variability, this shift is explained by AERO-driven thermodynamic and kinetic alterations (Li et al., 2016a, 2016b; Stier et al., 2024; Zhao et al., 2024). Specifically, aerosol particle concentrations influence radiative fluxes and cloud formation, further impacting the land-sea temperature gradient and local circulation patterns within monsoon regions (Patil et al., 2019). While GHG forcing induces atmospheric warming, its sensitivity within the hydroclimate cycle is lower compared to that of AERO forcing (Ayantika et al., 2021; Barnett et al., 2005). It is important to note that the fingerprint method may not be accurately modelled at local scales, and biases may arise in the splicing of past and future data. Furthermore, despite limitations in the spatial coverage and uncertainty (e.g. data sources) of the fingerprint experiment, this study provides an initial exploration into the anthropogenic mechanisms driving climate change in the NCMMR.

Pre-industrial control simulations in the CMIP6 model fingerprint offer more conservative estimates of internal variability and natural forcing contributions to precipitation changes (Sippel et al., 2021). Fingerprint experiments suggest that the impact of GHG forcing on precipitation will become stable and significant (*almost certainly*, 99 % confidence, 2025–2050) in the future (Fig. 8). Spatial fingerprint analysis using additional CRU precipitation grid data revealed a significant upward trend in GHG forcing since the 21st century (Supporting Information S4). Beyond North China, megadroughts occurring in the Americas have similarly been attributed to anthropogenic climate change (Cook et al., 2022; Steiger et al., 2021). Meanwhile, the influence of volcanic and solar forcings on precipitation variability in the NCMMR since the 20th century appears minimal, whereas orbital forcing operates on timescales exceeding interannual precipitation variability (Supporting Information S4). These findings indicate that anthropogenic forcing plays a critical role in shaping precipitation variability in the NCMMR. However, quantifying the isolated effects of GHG and AERO remains a challenging task. A deeper understanding of how these anthropogenic forcings interact with complex natural variability will be essential for improving future precipitation projections in the NCMMR.

## 5. Conclusions

Our annual precipitation reconstruction for the NCMMR, along with independent hydroclimatic records along the ASM pathway, reveals a widespread decline in precipitation since the mid-20th century. Results

from CESM-LME simulations and reanalysis data indicate that internal variability since 1770—including the IPO, AMO, IOD, and ENSO—has influenced precipitation changes. Fingerprint analysis identified a significant increase in the GHG forcing signal during the first half of the 20th century, with this signal becoming robustly detectable in the early 21st century. The subsequent reduction in the GHG forcing signal during the latter half of the 20th century is closely aligned with the trend observed in reconstructed precipitation. The persistent drying trend since the mid-20th century is likely driven by the teleconnection effects of the coupled atmosphere-ocean system and anthropogenic forcing. Anthropogenic influences are expected to exert an increasing influence on precipitation changes in North China over the coming decades.

## CRediT authorship contribution statement

**Xiaoen Zhao:** Writing – review & editing, Writing – original draft, Methodology, Investigation, Funding acquisition, Formal analysis, Conceptualization. **Chenxi Xu:** Writing – review & editing, Writing – original draft, Investigation, Formal analysis, Data curation, Conceptualization. **Feng Chen:** Writing – original draft, Supervision, Software, Resources, Methodology, Investigation, Data curation, Conceptualization. **Étienne Boucher:** Writing – review & editing, Writing – original draft, Validation, Project administration, Methodology, Investigation, Formal analysis, Data curation, Conceptualization. **Martín Hadad:** Software, Formal analysis, Data curation, Conceptualization. **Fidel A. Roig:** Writing – original draft, Visualization, Validation. **Jiafeng Xu:** Formal analysis, Data curation, Conceptualization. **Mao Hu:** Formal analysis, Data curation, Conceptualization. **Shijie Wang:** Formal analysis, Data curation, Conceptualization. **Heli Zhang:** Formal analysis, Data curation, Conceptualization. **Youping Chen:** Formal analysis, Data curation, Conceptualization. **Weipeng Yue:** Formal analysis, Data curation, Conceptualization. **Honghua Cao:** Formal analysis, Data curation, Conceptualization.

## Declaration of competing interest

The authors declare that they have no known competing financial interests or personal relationships that could have appeared to influence the work reported in this paper.

## Acknowledgements

This study is supported by National Key Research and Development Program of China (Grant Number: 2024YFF0807902), the National Natural Science Foundation of China (Grant Number: 32061123008), International Partnership program of the Chinese Academy of Sciences (Grant Number: 170GJHZ2023074GC), the Key Research Program of the Institute of Geology and Geophysics (CAS Grant IGGCAS-201905), CAS Youth Interdisciplinary Team (JCTD-2021-05) and the Yunnan University Research Innovation Fund for Graduate Students (KC-22222199). We thank all the collaborators who developed and shared the dataset to complete this work. We also thank the editors and anonymous reviewers who provided to some valuable suggestions.

## Appendix A. Supplementary data

Supplementary data to this article can be found online at <https://doi.org/10.1016/j.palaeo.2025.113180>.

## Data availability

The ERSST V5 dataset (Huang et al., 2017) provided by the NOAA at <https://psl.noaa.gov/data/gridded/data.noaa.ersst.v5.html>. The NCEP reanalysis dataset (Kalnay et al., 1996) can be obtained from <https://psl.noaa.gov/data/gridded/data.ncep.reanalysis.html>. The CESM-LME dataset (Otto-Bliesner et al., 2016) free download at <https://www>

[earthsystemgrid.org/dataset/ucar.cgd.ccsm4.cesmLME.html](https://earthsystemgrid.org/dataset/ucar.cgd.ccsm4.cesmLME.html). The CRU grid dataset (Harris et al., 2020) can be obtained from [https://crudata.uea.ac.uk/cru/data/hrg/cru\\_ts\\_4.07/cruts.2304141047.v4.07/pre/](https://crudata.uea.ac.uk/cru/data/hrg/cru_ts_4.07/cruts.2304141047.v4.07/pre/). The CMIP6 outputs are available from the Earth System Grid Federation (ESGF) at <https://esgf-data.dkrz.de/search/cmip6-dkrz/>. The Precipitation Grid Reconstruction dataset (Shi et al., 2017) can be obtained from <https://www.ncei.noaa.gov/pub/data/paleo/reconstructions/shi2017/>. The MADA dataset (Cook et al., 2010) free download at <http://iridl.ldeo.columbia.edu/SOURCES/LDEO/.TRL/.MADA/>. The IPO, ENSO, AMO, IOD indices, and reanalysis data can download at [https://psl.noaa.gov/site\\_index.html#](https://psl.noaa.gov/site_index.html#). The reconstructed precipitation and tree ring stable oxygen isotope data that support the results of this study are free download at <https://data.mendeley.com/datasets/rng92psg4h/1> (Doi: 10.17632/rng92psg4h.1).

## References

- Aihaiti, A., Jiang, Z., Li, Y., Tao, L., Zhu, L., Zhang, J., 2023. The global warming and IPO impacts on summer extreme precipitation in China. *Clim. Dyn.* 60 (11), 3369–3384. <https://doi.org/10.1007/s00382-022-06511-x>.
- Allen, S.T., Kirchner, J.W., Braun, S., Siegwolf, R.T., Goldsmith, G.R., 2019. Seasonal origins of soil water used by trees. *Hydrol. Earth Syst. Sci.* 23 (2), 1199–1210. <https://doi.org/10.5194/hess-23-1199-2019>.
- An, W., Xu, C., Marković, S.B., Sun, S., Sun, Y., Gavrilov, M.B., et al., 2023. Anthropogenic warming has exacerbated droughts in southern Europe since the 1850s. *Commun. Earth & Environ.* 4 (1), 232. <https://doi.org/10.1038/s43247-023-00907-1>.
- Antyikta, D.C., Krishnan, R., Singh, M., Swapna, P., Sandeep, N., Prajesh, A.G., et al., 2021. Understanding the combined effects of global warming and anthropogenic AERO forcing on the south Asian monsoon. *Clim. Dyn.* 56 (5), 1643–1662. <https://doi.org/10.1007/s00382-020-05551-5>.
- Babst, F., Poultier, B., Trouet, V., Tan, K., Neuwirth, B., Wilson, R., Frank, D., 2013. Site- and species-specific responses of forest growth to climate across the European continent. *Glob. Ecol. Biogeogr.* 22 (6), 706–717. <https://doi.org/10.1111/geb.12023>.
- Babst, F., Bouriaud, O., Poultier, B., Trouet, V., Girardin, M.P., Frank, D.C., 2019. Twentieth century redistribution in climatic drivers of global tree growth. *Sci. Adv.* 5 (1), eaat4313. <https://doi.org/10.1126/sciadv.aat4313>.
- Banerjee, D., Singh, C., 2022. An appraisal of seasonal precipitation dynamics over the North-West Himalayan region under future warming scenarios. *Int. J. Climatol.* 42 (4), 2328–2350.
- Barnett, T.P., Adam, J.C., Lettenmaier, D.P., 2005. Potential impacts of a warming climate on water availability in snow-dominated regions. *Nature* 438 (7066), 303–309. <https://doi.org/10.1038/nature04141>.
- Bathiyan, S., Dijkstra, H., Crucifix, M., Dakos, V., Brovkin, V., Williamson, M.S., et al., 2016. Beyond bifurcation: using complex models to understand and predict abrupt climate change. *Dynamics and Statistics of the climate. System* 1 (1), dzw004. <https://doi.org/10.1093/climys/dzw004>.
- Battipaglia, G., Jäaggi, M., Saurer, M., Siegwolf, R.T.W., Cotrufo, M.F., 2008. Climatic sensitivity of  $\delta^{18}\text{O}$  in the wood and cellulose of tree rings: results from a mixed stand of *Acer pseudoplatanus* L. and *Fagus sylvatica* L. *Palaeogeogr. Palaeoclimatol. Palaeoecol.* 261 (1), 193–202. <https://doi.org/10.1016/j.palaeo.2008.01.020>.
- Baxter, A.J., Verschuren, D., Peterse, F., Miralles, D.G., Martin-Jones, C.M., Maitituerdi, A., Sinnighe Damsté, J.S., 2023. Reversed Holocene temperature–moisture relationship in the Horn of Africa. *Nature* 620 (7973), 336–343. <https://doi.org/10.1038/s41586-023-06272-5>.
- Bindoff, N., 2013. In: Stocker, T.F., et al. (Eds.), Coauthors, 2013: Detection and attribution of climate change: from global to regional. *Climate Change 2013: The Physical Science Basis*. Cambridge University Press.
- Bollasina, M.A., Messori, G., 2018. On the link between the subseasonal evolution of the North Atlantic Oscillation and East Asian climate. *Clim. Dyn.* 51 (9), 3537–3557. <https://doi.org/10.1007/s00382-018-4095-5>.
- Bonfils, C.J.W., Santer, B.D., Fyfe, J.C., Marvel, K., Phillips, T.J., Zimmerman, S.R.H., 2020. Human influence on joint changes in temperature, rainfall and continental aridity. *Nat. Clim. Chang.* 10 (8), 726–731. <https://doi.org/10.1038/s41558-020-0821-1>.
- Bradley, R.S., Briffa, K.R., Cole, J., Hughes, M.K., Osborn, T.J., 2003. The climate of the last millennium. Paleoclimate, global change and the future 105–141. [https://doi.org/10.1007/978-3-642-55828-3\\_6](https://doi.org/10.1007/978-3-642-55828-3_6).
- Buckley, B.M., Fletcher, R., Wang, S.-Y.S., Zottoli, B., Pottier, C., 2014. Monsoon extremes and society over the past millennium on mainland Southeast Asia. *Quat. Sci. Rev.* 95, 1–19. <https://doi.org/10.1016/j.quascirev.2014.04.022>.
- Cai, W., Wang, G., Santoso, A., McPhaden, M.J., Wu, L., Jin, F.-F., et al., 2015. Increased frequency of extreme La Niña events under greenhouse warming. *Nat. Clim. Chang.* 5 (2), 132–137. <https://doi.org/10.1038/nclimate2492>.
- Cai, Q., Liu, Y., Fang, C., Xie, M., Zhang, H., Li, Q., et al., 2022. Insight into spatial-temporal patterns of hydroclimate change on the Chinese Loess Plateau over the past 250 years, using new evidence from tree rings. *Sci. Total Environ.* 850, 157960. <https://doi.org/10.1016/j.scitotenv.2022.157960>.
- Chen, F., Opala-Owczarek, M., Owczarek, P., Chen, Y., 2020. Summer monsoon season streamflow variations in the Middle Yellow River since 1570 CE inferred from tree rings of *Pinus tabulaeformis*. *Atmosphere* 11 (7). <https://doi.org/10.3390/atmos1107071>.
- Cao, H., Chen, F., Hu, M., Hou, T., Zhao, X., Wang, S., et al., 2025. Tree-ring insights into past and future streamflow variations in Beijing, northern China. *Water Resour. Res.* 61 (1). <https://doi.org/10.1029/2024WR038084>.
- Chen, J., Li, X., Martel, J.L., Brisette, F.P., Zhang, X.J., Frei, A., 2021. Relative importance of internal climate variability versus anthropogenic climate change in global climate change. *J. Clim.* 34 (2), 465–478. <https://doi.org/10.1175/JCLI-D-20-0424.1>.
- Chen, F., Wang, T., Zhao, X., Esper, J., Ljungqvist, F.C., Büntgen, U., Linderholm, H.W., Meko, D., Xu, H., Yue, W., 2024. Coupled pacific rim megadroughts contributed to the fall of the ming Dynasty's capital in 1644 CE. *Sci. Bull.* 69, 3106–3114.
- Chen, F., Yuan, Y., Trouet, V., Büntgen, U., Esper, J., Chen, F., et al., 2022. Ecological and societal effects of Central Asian streamflow variation over the past eight centuries. *npj clim. Atmos. Sci.*, 5 (1), 27. <https://doi.org/10.1038/s41612-022-00239-5>.
- Chen, F., Man, W., Wang, S., Esper, J., Meko, D., Büntgen, U., et al., 2023a. Southeast Asian ecological dependency on Tibetan Plateau streamflow over the last millennium. *Nat. Geosci.* 16 (12), 1151–1158. <https://doi.org/10.1038/s41561-023-01320-1>.
- Chen, Q., Zhang, X., Chen, F., Zhang, H., Yuan, Y., Yu, S., et al., 2023b. Weakening of the Summer Monsoon over the past 150 years Shown by a Tree-Ring Record from Shandong, Eastern China, and the potential Role of North Atlantic climate. *Paleoceanogr. Paleoclimatol.* 38 (3). <https://doi.org/10.1029/2022PA004495>.
- Cisneros, M., Cacho, I., Moreno, A., Stoll, H., Torner, J., Català, A., Fornós, J.J., 2021. Hydroclimate variability during the last 2700 years based on stalagmite multi-proxy records in the Central-Western Mediterranean. *Quat. Sci. Rev.* 269, 107137. <https://doi.org/10.1016/j.quascirev.2021.107137>.
- Collins, M., The, C.M.G., 2005. El Niño- or La Niña-like climate change? *Clim. Dyn.* 24 (1), 89–104. <https://doi.org/10.1007/s00382-004-0478-x>.
- Collins, W.J., Lamarque, J.F., Schulz, M., Boucher, O., Eyring, V., Hegglin, M.I., et al., 2017. AerChemMP: quantifying the effects of chemistry and AEROS in CMIP6. *Geosci. Model Dev.* 10 (2), 585–607. <https://doi.org/10.5194/gmd-10-585-2017>.
- Cook, E.R., 1985. *Arstan (Computer Program)*. Columbia University, New York, NY.
- Cook, E.R., Anchukaitis, K.J., Buckley, B.M., D'Arrigo, R.D., Jacoby, G.C., Wright, W.E., 2010. Asian Monsoon failure and Megadrought during the last Millennium [Dataset]. *Science* 328 (5977), 486–489. <https://doi.org/10.1126/science.1185188>.
- Cook, B.I., Smerdon, J.E., Cook, E.R., Williams, A.P., Anchukaitis, K.J., Mankin, J.S., et al., 2022. Megadroughts in the Common Era and the Anthropocene. *Nat. Rev. Earth & Environ.* 3 (11), 741–757. <https://doi.org/10.1038/s43017-022-00329-1>.
- Danabasoglu, G., Lamarque, J.F., Bacmeister, J., Bailey, D.A., DuVivier, A.K., Edwards, J., et al., 2020. The Community Earth System Model Version 2 (CESM2). *J. Adv. Model. Earth Systems* 12 (2). <https://doi.org/10.1029/2019MS001916> e2019MS001916.
- Dansgaard, W., 1964. Stable isotopes in precipitation. *Tellus* 16 (4), 436–468.
- Deng, Y., 2020. *The History of Famine Relief in China*. Cambridge University Press.
- Deng, Y., Gao, T., Gao, H., Yao, X., Xie, L., 2014. Regional precipitation variability in East Asia related to climate and environmental factors during 1979–2012. *Sci. Rep.* 4 (1), 5693. <https://doi.org/10.1038/srep05693>.
- Ding, G., Chen, J., Yan, H., Zhang, S., Liu, Y., Zhou, A., et al., 2022. Late Holocene transition from natural to anthropogenic forcing of vegetation change in the semi-arid region of northern China. *Quat. Sci. Rev.* 287, 107561. <https://doi.org/10.1016/j.quascirev.2022.107561>.
- Dong, H., Huang, S., Wang, H., Shi, H., Singh, V.P., She, D., et al., 2024. Effects of interaction of multiple large-scale atmospheric circulations on precipitation dynamics in China. *Sci. Total Environ.* 923, 171528. <https://doi.org/10.1016/j.scitotenv.2024.171528>.
- Enfield, D.B., Mestas-Nuñez, A.M., Trimble, P.J., 2001. The Atlantic multidecadal oscillation and its relation to rainfall and river flows in the continental US [Dataset]. *Geophys. Res. Lett.* 28 (10), 2077–2080. <https://doi.org/10.1029/2000GL012745>.
- Fan, H., Gou, X., Nakatsuka, T., Li, Z., Fang, K., Su, J., et al., 2022. Different moisture regimes during the last 150 years inferred from a tree-ring  $\delta^{18}\text{O}$  network over the transitional zone of the Asian summer monsoon. *J. Hydrol.* 613, 128484. <https://doi.org/10.1016/j.jhydrol.2022.128484>.
- Freund, M.B., Helle, G., Balting, D.F., Ballis, N., Schleser, G.H., Cubasch, U., 2023. European tree-ring isotopes indicate unusual recent hydroclimate. *Commun. Earth & Environ.* 4 (1), 26. <https://doi.org/10.1038/s43247-022-00648-7>.
- Galewsky, J., Steen-Larsen, H.C., Field, R.D., Worden, J., Risi, C., Schneider, M., 2016. Stable isotopes in atmospheric water vapor and applications to the hydrologic cycle. *Rev. Geophys.* 54 (4), 809–865. <https://doi.org/10.1002/2015RG000512>.
- Gao, Y., Li, Z., Zhu, R., 2022. Holocene Millennial-Scale Precipitation Variations in the Asian Summer Monsoon margin of Northwest China and their Relation to Migrations of Monsoon Northern Boundary via Oxygen Isotope Analysis of Calcareous root Tubes in Deserts. *J. Geophys. Res. Atmos.* 127 (4). <https://doi.org/10.1029/2021JD035815> e2021JD035815.
- Ge, Q., Zheng, J., Hao, Z., Liu, Y., Li, M., 2016. Recent advances on reconstruction of climate and extreme events in China for the past 2000 years. *J. Geogr. Sci.* 26 (7), 827–854. <https://doi.org/10.1007/s11442-016-1301-4>.
- Gessler, A., Ferri, J.P., Hommel, R., Treyte, K., Werner, R.A., Monson, R.K., 2014. Stable isotopes in tree rings: towards a mechanistic understanding of isotope fractionation and mixing processes from the leaves to the wood. *Tree Physiol.* 34 (8), 796–818. <https://doi.org/10.1093/treephys/tpu040>.
- Giguère, C., Boucher, É., Bergeron, Y., 2016. Multicentury reconstruction of precipitations (1300–2014) in Eastern Canada from tree-ring width and carbon and oxygen isotopes. In: EGU General Assembly Conference Abstracts (pp. EPSC2016-5141).

- Gimeno, L., Stohl, A., Trigo, R.M., Dominguez, F., Yoshimura, K., Yu, L., Nieto, R., 2012. Oceanic and terrestrial sources of continental precipitation. *Rev. Geophys.* 50 (4). <https://doi.org/10.1029/2012RG000389>.
- Griesinger, J., Bräuning, A., Helle, G., Thomas, A., Schleser, G., 2011. Late Holocene Asian summer monsoon variability reflected by  $\delta^{18}\text{O}$  in tree-rings from Tibetan junipers. *Geophys. Res. Lett.* 38 (3). <https://doi.org/10.1029/2010GL045988>.
- Guo, Q., 1983. The summer monsoon intensity index in East Asia and its variation (in Chinese). *Acta Geograph. Sin.* 38 (3), 207–216.
- Hacket-Pain, A.J., Ascoli, D., Vacchiano, G., Biondi, F., Cavin, L., Conedera, M., Zang, C. S., 2018. Climatically controlled reproduction drives interannual growth variability in a temperate tree species. *Ecol. Lett.* 21 (12), 1833–1844. <https://doi.org/10.1111/ele.13158>.
- Hammond, W.M., Williams, A.P., Abatzoglou, J.T., Adams, H.D., Klein, T., López, R., Allen, C.D., 2022. Global field observations of tree die-off reveal hotter-drought fingerprint for Earth's forests. *Nat. Commun.* 13 (1), 1761. <https://doi.org/10.1038/s41467-022-29289-2>.
- Han, T., He, S., Hao, X., Wang, H., 2018. Recent interdecadal shift in the relationship between Northeast China's winter precipitation and the North Atlantic and Indian Oceans. *Clim. Dyn.* 50, 1413–1424. <https://doi.org/10.1007/s00382-017-3694-x>.
- Han, X., Li, Y., Liu, F., Li, J., Zheng, X., Li, Y., et al., 2023. Stability of ENSO teleconnections during the last millennium in CESM. *Clim. Dyn.* 61 (11), 5699–5714. <https://doi.org/10.1007/s00382-023-06878-5>.
- Harris, I., Osborn, T.J., Jones, P., Lister, D., 2020. Version 4 of the CRU TS monthly high-resolution gridded multivariate climate dataset [dataset]. *Sci. Data* 7 (1), 109. <https://doi.org/10.1038/s41597-020-0453-3>.
- Hasselmann, K., 1997. Multi-pattern fingerprint method for detection and attribution of climate change. *Clim. Dyn.* 13 (9), 601–611. <https://doi.org/10.1007/s003820050185>.
- Hegerl, G.C., Brönnimann, S., Cowan, T., Friedman, A.R., Hawkins, E., Iles, C., 2019. Causes of climate change over the historical record. *Environ. Res. Lett.* 14 (12), 123006. <https://doi.org/10.1088/1748-9326/ab4557>.
- Henley, B.J., Gergis, J., Karoly, D.J., Power, S.B., Kennedy, J., Folland, C.K., 2015. A Tripole Index for the Interdecadal Pacific Oscillation [Dataset]. *Clim. Dyn.* 45 (11–12), 3077–3090. <https://doi.org/10.1007/s00382-015-2525-1>.
- Hernández, A., Martín-Puertas, C., Moffa-Sánchez, P., Moreno-Chamarro, E., Ortega, P., Blockley, S., 2020. Modes of climate variability: Synthesis and review of proxy-based reconstructions through the Holocene. *Earth Sci. Rev.* 209, 103286. <https://doi.org/10.1016/j.earscirev.2020.103286>.
- Herzschuh, U., Cao, X., Laepple, T., Dallmeyer, A., Telford, R.J., Ni, J., Zheng, Z., 2019. Position and orientation of the westerly jet determined Holocene rainfall patterns in China. *Nat. Commun.* 10 (1), 2376. <https://doi.org/10.1038/s41467-019-09866-8>.
- Holmes, R.L., 1983. Computer-Assisted Quality Control in Tree-Ring Dating and Measurement.
- Hu, J., Dee, S., Parajuli, G., Thirumalai, K., 2023. Tropical Pacific modulation of the Asian summer monsoon over the last millennium in paleoclimate data assimilation reconstructions. *J. Geophys. Res. Atmos.* 128 (20) e2023JD039207.
- Huang, J., Tardif, J.C., Bergeron, Y., Dennerle, B., Berninger, F., Girardin, M.P., 2010. Radial growth response of four dominant boreal tree species to climate along a latitudinal gradient in the eastern Canadian boreal forest. *Glob. Chang. Biol.* 16 (2), 711–731. <https://doi.org/10.1111/j.1365-2486.2009.01990.x>.
- Huang, B., Thorne, P.W., Banzon, V.F., Boyer, T., Chepurin, G., Lawrimore, J.H., et al., 2017. NOAA extended reconstructed sea surface temperature (ERSST), version 5 [Dataset]. NOAA Nat. Centers for Environ. Inform. <https://doi.org/10.7289/V5T72FNM>.
- Hughes, M.K., Xiang, W., Xuemei, S., Garfin, G.M., 1994. A preliminary reconstruction of rainfall in north-Central China since AD 1600 from tree-ring density and width. *Quat. Res.* 42 (1), 88–99. <https://doi.org/10.1006/qres.1994.1056>.
- Johnston, V.E., Borsato, A., Frisia, S., Spötl, C., Hellstrom, J.C., Cheng, H., Edwards, R.L., 2021. Last interglacial hydroclimate in the Italian Prealps reconstructed from speleothem multi-proxy records (Bigonda Cave, NE Italy). *Quat. Sci. Rev.* 272, 107243. <https://doi.org/10.1016/j.quascirev.2021.107243>.
- Kalnay, E., Kanamitsu, M., Kistler, R., Collins, W., Deaven, D., Gandin, L., et al., 1996. The NCEP/NCAR 40-year reanalysis project [Dataset]. *Bull. Am. Meteorol. Soc.* 77 (3), 437–471. [https://doi.org/10.1175/1520-0477\(1996\)077<0437:TNYRP>2.0.CO;2](https://doi.org/10.1175/1520-0477(1996)077<0437:TNYRP>2.0.CO;2).
- Kang, S., Yang, B., 2015. Precipitation variability at the northern fringe of the Asian summer monsoon in northern China and its possible mechanism over the past 53 years. *Quaternary Sci.* 35 (5), 1185–1193. <https://doi.org/10.11928/j.issn.1001-7410.2015.05.14>.
- Kathayat, G., Sinha, A., Breitenbach, S.F.M., Tan, L., Spötl, C., Li, H., et al., 2022. Protracted Indian monsoon droughts of the past millennium and their societal impacts. *Proc. Natl. Acad. Sci.* 119 (39), e2207487119. <https://doi.org/10.1073/pnas.2207487119>.
- Kerr, R.A., 2000. A North Atlantic climate pacemaker for the centuries. *Science* 288 (5473), 1984–1985. <https://doi.org/10.1126/science.288.5473.1984>.
- Kumar, P.V., Naidu, C.V., Prasanna, K., 2020. Recent unprecedented weakening of Indian summer monsoon in warming environment. *Theor. Appl. Climatol.* 140 (1), 467–486. <https://doi.org/10.1007/s00704-019-03087-1>.
- Kurita, N., Nakatsuka, T., Ohnishi, K., Mitsutani, T., Kumagai, T.O., 2016. Analysis of the interdecadal variability of summer precipitation in Central Japan using a reconstructed 106 year long oxygen isotope record from tree ring cellulose. *J. Geophys. Res. Atmos.* 121 (20), 12–089. <https://doi.org/10.1002/2016JD025463>.
- Labotka, D.M., Grissino-Mayer, H.D., Mora, C.I., Johnson, E.J., 2016. Patterns of moisture source and climate variability in the southeastern United States: a four-century seasonally resolved tree-ring oxygen-isotope record. *Clim. Dyn.* 46 (7), 2145–2154. <https://doi.org/10.1007/s00382-015-2694-y>.
- Laubuhn, I., Daux, V., Pierre, M., Stievenard, M., Girardclos, O., Féron, A., et al., 2014. Tree age, site and climate controls on tree ring cellulose  $\delta^{18}\text{O}$ : a case study on oak trees from South-Western France. *Dendrochronologia* 32 (1), 78–89. <https://doi.org/10.1016/j.dendro.2013.11.001>.
- Laepple, T., Ziegler, E., Weitzel, N., Hébert, R., Ellerhoff, B., Schoch, P., 2023. Regional but not global temperature variability underestimated by climate models at supradecadal timescales. *Nat. Geosci.* 16 (11), 958–966. <https://doi.org/10.1038/s41561-023-01299-9>.
- Li, Q., Nakatsuka, T., Kawamura, K., Liu, Y., Song, H., 2011a. Hydroclimate variability in the North China Plain and its link with El Niño–Southern Oscillation since 1784 AD: Insights from tree-ring cellulose  $\delta^{18}\text{O}$ . *J. Geophys. Res. Atmos.* 116 (D22). <https://doi.org/10.1029/2011JD015987>.
- Li, Q., Nakatsuka, T., Kawamura, K., Liu, Y., Song, H., 2011b. Regional hydroclimate and precipitation  $\delta^{18}\text{O}$  revealed in tree-ring cellulose  $\delta^{18}\text{O}$  from different tree species in semi-arid Northern China. *Chem. Geol.* 282 (1–2), 19–28. <https://doi.org/10.1016/j.chemgeo.2011.01.004>.
- Li, Y., Chen, F., Zhao, X., Yue, W., Hu, M., Niu, J., et al., 2025. Precipitation reconstruction for the western Chinese Loess Plateau since 1598 CE reveals recent wetting signals. *Palaeogeogr. Palaeoclimatol. Palaeoecol.* 668, 112898. <https://doi.org/10.1016/j.palaeo.2025.112898>.
- Li, Z., Lau, W.K.M., Ramanathan, V., Wu, G., Ding, Y., Manoj, M.G., et al., 2016a. AERO and monsoon climate interactions over Asia. *Rev. Geophys.* 54 (4), 866–929. <https://doi.org/10.1002/2015RG000500>.
- Li, Z., Lau, W.M., Ramanathan, V., Wu, G., Ding, Y., Manoj, M.G., et al., 2016b. AERO and monsoon climate interactions over Asia. *Rev. Geophys.* 54 (4), 866–929. <https://doi.org/10.1002/2015RG000500>.
- Li, Q., Liu, Y., Nakatsuka, T., Fang, K., Song, H., Liu, R., et al., 2019. East Asian Summer Monsoon moisture sustains summer relative humidity in the southwestern Gobi Desert, China: evidence from  $\delta^{18}\text{O}$  of tree rings. *Clim. Dyn.* 52 (11), 6321–6337. <https://doi.org/10.1007/s00382-018-4515-6>.
- Li, Q., Liu, Y., Nakatsuka, T., Zhang, Q.B., Ohnishi, K., Sakai, A., et al., 2020. Oxygen stable isotopes of a network of shrubs and trees as high-resolution paleoclimatic proxies in Northwestern China. *Agric. For. Meteorol.* 285, 107929. <https://doi.org/10.1016/j.agrformet.2020.107929>.
- Li, Q., Liu, Y., Meko, D.M., Nakatsuka, T., Pan, Y., Song, H., et al., 2022. Water resource management implications for a desert oasis from tree-ring  $\delta^{18}\text{O}$  variations in *Populus euphratica* in Northwest China. *Water Resour. Res.* 58 (4). <https://doi.org/10.1029/2022WR031953>.
- Li, Y., Zeng, X., Liu, X., Evans, M.N., Xu, G., Szejner, P., Ni, P., 2023. A seasonally varying tree physiological response to environmental conditions: results from semi-arid China. *Journal of Geophysical Research: Biogeosciences* 128 (7). <https://doi.org/10.1029/2023JG007455>.
- Li, G., Yu, Z., Li, Y., Yang, C., Gu, H., Zhang, J., Huang, Y., 2024. Interaction mechanism of global multiple ocean-atmosphere coupled modes and their impacts on South and East Asian Monsoon: a review. *Glob. Planet. Chang.* 104438. <https://doi.org/10.1016/j.gloplacha.2024.104438>.
- Liang, E., Liu, X., Yuan, Y., Qin, N., Fang, X., Huang, L., et al., 2006. The 1920S Drought Recorded by tree Rings and Historical documents in the Semi-Arid and Arid areas of Northern China. *Clim. Chang.* 79 (3), 403–432. <https://doi.org/10.1007/s10584-006-9082-x>.
- Liang, Y., Zhao, X., Chen, F., Yang, Y., Ljungqvist, F.C., 2025. Winter-spring drought in Yunnan since the early 19th century and its impact on social governance in China's southwestern border regions. *Humanit. Soc. Sci. Commun.* 12 (1), 1–15. <https://doi.org/10.1057/s41599-025-05356-z>.
- Littell, J.S., Peterson, D.L., Tjoelker, M., 2008. Douglas-fir growth in mountain ecosystems: water limits tree growth from stand to region. *Ecol. Monogr.* 78 (3), 349–368. <https://doi.org/10.1890/07-0712.1>.
- Liu, L., Li, Z., Yang, X., Gong, H., Li, C., Xiong, A., 2016. The long-term trend in the diurnal temperature range over Asia and its natural and anthropogenic causes. *J. Geophys. Res. Atmos.* 121 (7), 3519–3533. <https://doi.org/10.1002/2015JD024549>.
- Liu, Y., Wang, L., Li, Q., Cai, Q., Song, H., Sun, C., et al., 2019a. Asian Summer Monsoon-Related Relative Humidity Recorded by tree Ring  $\delta^{18}\text{O}$  during last 205 years. *J. Geophys. Res. Atmos.* 124 (17–18), 9824–9838. <https://doi.org/10.1029/2019JD030512>.
- Liu, Y., Cai, W., Sun, C., Song, H., Cobb, K.M., Li, J., et al., 2019b. Anthropogenic AEROS Cause recent Pronounced weakening of Asian Summer Monsoon Relative to last four Centuries. *Geophys. Res. Lett.* 46 (10), 5469–5479. <https://doi.org/10.1029/2019GL082497>.
- Liu, Y., Shi, W., Li, Q., Liu, W., Cai, Q., 2022. A 230-year summer precipitation variations recorded by tree-ring  $\delta^{18}\text{O}$  in Heng Mountains, North China. *Forests* 13 (10), 1654. <https://doi.org/10.3390/f13101654>.
- Loader, N.J., McCarroll, D., Gagen, M., Robertson, I., Jalkanen, R., 2007. Extracting climatic information from stable isotopes in tree rings. *Terrestrial Ecol.* 1, 25–48. [https://doi.org/10.1016/S1936-7961\(07\)01003-2](https://doi.org/10.1016/S1936-7961(07)01003-2).
- Macumber, A.L., Patterson, R.T., Galloway, J.M., Falck, H., Swindles, G.T., 2018. Reconstruction of Holocene hydroclimatic variability in subarctic treeline lakes using lake sediment grain-size end-members. *The Holocene* 28 (6), 845–857. <https://doi.org/10.1177/0959683617752836>.
- Madakumbura, G.D., Thackeray, C.W., Norris, J., Goldenson, N., Hall, A., 2021. Anthropogenic influence on extreme precipitation over global land areas seen in multiple observational datasets. *Nat. Commun.* 12 (1), 3944. <https://doi.org/10.1038/s41467-021-24262-x>.
- Marvel, K., Cook, B.I., Bonfils, C.J.W., Durack, P.J., Smerdon, J.E., Williams, A.P., 2019. Twentieth-century hydroclimate changes consistent with human influence. *Nature* 569 (7754), 59–65. <https://doi.org/10.1038/s41586-019-1149-8>.

- McCarroll, D., Loader, N.J., 2004. Stable isotopes in tree rings. *Quat. Sci. Rev.* 23 (7–8), 771–801. <https://doi.org/10.1016/j.quascirev.2003.06.017>.
- Otto-Biesner, B.L., Brady, E.C., Fasullo, J., Jahn, A., Landrum, L., Stevenson, S., et al., 2016. Climate variability and change since 850 CE: An ensemble approach with the Community Earth System Model [Dataset]. *Bull. Am. Meteorol. Soc.* 97 (5), 735–754. <https://doi.org/10.1175/bams-d-14-00233.1>.
- Paik, S., Min, S.K., Zhang, X., Donat, M.G., King, A.D., Sun, Q., 2020. Determining the anthropogenic greenhouse gas contribution to the observed intensification of extreme precipitation. *Geophys. Res. Lett.* 47 (12) e2019GL086875.
- Palmer, P.I., Wainwright, C.M., Dong, B., Maidment, R.I., Wheeler, K.G., Gedney, N., et al., 2023. Drivers and impacts of Eastern African rainfall variability. *Nat. Rev. Earth & Environ.* 4 (4), 254–270. <https://doi.org/10.1038/s43017-023-00397-x>.
- Pandey, U., Nakatsuka, T., Mehrotra, N., Zhen, L., Kato, Y., Sano, M., Shah, S.K., 2023. Tree-rings stable isotope ( $\delta^{18}\text{O}$  and  $\delta^{2\text{H}}$ ) based 368 years long term precipitation reconstruction of South Eastern Kashmir Himalaya. *Sci. Total Environ.* 892, 164640. <https://doi.org/10.1016/j.scitotenv.2023.164640>.
- Patil, N., Venkataraman, C., Muduchuru, K., Ghosh, S., Mondal, A., 2019. Disentangling Sea-surface temperature and anthropogenic AERO influences on recent trends in south Asian monsoon rainfall. *Clim. Dyn.* 52 (3), 2287–2302. <https://doi.org/10.1007/s00382-018-4251-y>.
- Peng, J., Peng, K., Li, X., Peng, M., Li, J., Wei, X., et al., 2024. Tree-ring widths of *Pinus tabulaeformis* Carr reveal variability of winter half-year precipitation on the north-south transition zone in Central China over the past 220 years. *Sci. Total Environ.* 931, 172719. <https://doi.org/10.1016/j.scitotenv.2024.172719>.
- Prentice, I.C., Villegas-Diaz, R., Harrison, S.P., 2022. Accounting for atmospheric carbon dioxide variations in pollen-based reconstruction of past hydroclimates. *Glob. Planet. Chang.* 211, 103790. <https://doi.org/10.1016/j.gloplacha.2022.103790>.
- Qiu, Y., Cai, W., Guo, X., Ng, B., 2014. The asymmetric influence of the positive and negative IOD events on China's rainfall. *Sci. Rep.* 4 (1), 4943. <https://doi.org/10.1038/srep04943>.
- Qu, L., Zhao, Y., Yao, J., Meng, L., 2024. Interdecadal variability in the dominant synoptic patterns responsible for the summer daily extreme precipitation over the Tarim Basin, Northwest China. *Atmosph. Res.* 312, 107746. <https://doi.org/10.1016/j.atmosres.2024.107746>.
- Raihani, N., Aitken, D., 2011. Uncertainty, rationality and cooperation in the context of climate change. *Clim. Chang.* 108 (1), 47–55. <https://doi.org/10.1007/s10584-010-0014-4>.
- Rayner, N.A.A., Parker, D.E., Horton, E.B., Folland, C.K., Alexander, L.V., Rowell, D.P., et al., 2003. Global analyses of sea surface temperature, sea ice, and night marine air temperature since the late nineteenth century [Dataset]. *J. Geophys. Res. Atmos.* 108 (D14). <https://doi.org/10.1029/2002JD002670>.
- Reis, L.S., Boulobassi, I., Mendez-Millan, M., Guimaraes, J.T.F., de Araújo Romeiro, L., Sahoo, P.K., Pessenda, L.C.R., 2022. Hydroclimate and vegetation changes in southeastern Amazonia over the past ~ 25,000 years. *Quat. Sci. Rev.* 284, 107466. <https://doi.org/10.1016/j.quascirev.2022.107466>.
- Rinne, K.T., Loader, N.J., Switsur, V.R., Waterhouse, J.S., 2013. 400-year May–August precipitation reconstruction for Southern England using oxygen isotopes in tree rings. *Quat. Sci. Rev.* 60, 13–25. <https://doi.org/10.1016/j.quascirev.2012.10.048>.
- Risser, M.D., Collins, W.D., Wehner, M.F., O'Brien, T.A., Huang, H., Ullrich, P.A., 2024. Anthropogenic AEROS mask increases in US rainfall by greenhouse gases. *Nat. Commun.* 15 (1), 1318.
- Roesch, C.M., Ballinger, A.P., Schurer, A.P., Hegerl, G.C., 2024. Combining temperature and precipitation to constrain the AERO contribution to observed climate change. *J. Clim.* <https://doi.org/10.1175/JCLI-D-23-0347.1>.
- Rosenzweig, C., Neofotis, P., 2013. Detection and attribution of anthropogenic climate change impacts. *Wiley Interdiscip. Rev. Clim. Chang.* 4 (2), 121–150. <https://doi.org/10.1002/wcc.209>.
- Saji, N.H., Goswami, B.N., Vinayachandran, P.N., Yamagata, T., 1999. A dipole mode in the tropical Indian Ocean. *Nature* 401 (6751), 360–363. <https://doi.org/10.1038/43854>.
- Saji, N.H., Yamagata, T.J.C.R., 2003. Possible impacts of Indian Ocean dipole mode events on global climate [Dataset]. *Clim. Res.* 25 (2), 151–169. <https://doi.org/10.3354/cr025151>.
- Santer, B.D., Mears, C., Doutriaux, C., Caldwell, P., Gleckler, P.J., Wigley, T.M.L., et al., 2011. Separating signal and noise in atmospheric temperature changes: The importance of timescale. *J. Geophys. Res. Atmos.* 116 (D22). <https://doi.org/10.1029/2011JD016263>.
- Santer, B.D., Painter, J.F., Mears, C.A., Doutriaux, C., Caldwell, P., Arblaster, J.M., et al., 2013. Identifying human influences on atmospheric temperature. *Proc. Natl. Acad. Sci.* 110 (1), 26–33. <https://doi.org/10.1073/pnas.1210514109>.
- Sarojini, B.B., Stott, P.A., Black, E., 2016. Detection and attribution of human influence on regional precipitation. *Nat. Clim. Chang.* 6 (7), 669–675. <https://doi.org/10.1038/nclimate2976>.
- Savard, M.M., Daux, V., 2020. An overview on isotopic divergences—causes for instability of tree-ring isotopes and climate correlations. *Clim. Past* 16 (4), 1223–1243. <https://doi.org/10.5194/cp-16-1223-2020>.
- Schllesinger, M., Ramankutty, N., 1994. An oscillation in the global climate system of period 65–70 years. *Nature* 367, 723–726. <https://doi.org/10.1038/367723a0>.
- Schollaen, K., Heinrich, I., Neuwirth, B., Krusic, P.J., D'Arrigo, R.D., Karyanto, O., Helle, G., 2013. Multiple tree-ring chronologies (ring width,  $\delta^{13}\text{C}$  and  $\delta^{18}\text{O}$ ) reveal dry and rainy season signals of rainfall in Indonesia. *Quat. Sci. Rev.* 73, 170–181. <https://doi.org/10.1016/j.quascirev.2013.05.018>.
- Schollaen, K., Baschek, H., Heinrich, I., Slotta, F., Pauly, M., Helle, G., 2017. A guideline for sample preparation in modern tree-ring stable isotope research. *Dendrochronologia* 44, 133–145. <https://doi.org/10.1016/j.dendro.2017.05.002>.
- Schott, F.A., Xie, S.-P., McCreary Jr., J.P., 2009. Indian Ocean circulation and climate variability. *Rev. Geophys.* 47 (1). <https://doi.org/10.1029/2007RG000245>.
- Sha, L., Wassenburg, J.A., Sha, L., Li, Y., Zhou, S., Liang, Q., et al., 2023. Variations in triple oxygen isotope of speleothems from the Asian monsoon region reveal moisture sources over the past 300 years. *Commun. Earth & Environ.* 4 (1), 384. <https://doi.org/10.1038/s43247-023-01043-6>.
- Shekhar, M., Sharma, A., Dimri, A.P., Tandon, S.K., 2022. Asian summer monsoon variability, global teleconnections, and dynamics during the last 1,000 years. *Earth Sci. Rev.* 230, 104041. <https://doi.org/10.1016/j.earscirev.2022.104041>.
- Shi, F., Li, J., Wilson, R.J., 2014. A tree-ring reconstruction of the south Asian summer monsoon index over the past millennium. *Sci. Rep.* 4 (1), 6739. <https://doi.org/10.1038/srep06739>.
- Shi, F., Zhao, S., Guo, Z., Goosse, H., Yin, Q., 2017. Multi-proxy reconstructions of May–September precipitation field in China over the past 500 years [Dataset]. *Clim. Past* 13 (12), 1919–1938. <https://doi.org/10.5194/cp-13-1919-2017>.
- Si, D., Jiang, D., Ding, Y., 2021. Synergistic impacts of the Atlantic and Pacific Oceans on interdecadal variations of summer rainfall in Northeast Asia. *J. Meteorol. Res.* 35 (5), 844–856. <https://doi.org/10.1007/s13351-021-0191-2>.
- Singh, D., Tsiang, M., Rajaratnam, B., Diffenbaugh, N.S., 2014. Observed changes in extreme wet and dry spells during the south Asian summer monsoon season. *Nat. Clim. Chang.* 4 (6), 456–461. <https://doi.org/10.1038/nclimate2208>.
- Singh, J., Singh, N., Chauhan, P., Yadav, R.R., Bräuning, A., Mayr, C., Rastogi, T., 2019. Tree-ring  $\delta^{18}\text{O}$  records of abating June–July monsoon rainfall over the Himalayan region in the last 273 years. *Quat. Int.* 532, 48–56. <https://doi.org/10.1016/j.quaint.2019.09.030>.
- Sippel, S., Meinshausen, N., Székely, E., Fischer, E., Pendergrass, A.G., Lehner, F., Knutti, R., 2021. Robust detection of forced warming in the presence of potentially large climate variability. *Science Advances* 7 (43), eabh4429.
- Song, F., Zhou, T., Qian, Y., 2014. Responses of East Asian summer monsoon to natural and anthropogenic forcings in the 17 latest CMIP5 models. *Geophys. Res. Lett.* 41 (2), 596–603. <https://doi.org/10.1002/2013GL058705>.
- Song, X., Zhang, C., Zhang, J., Zou, X., Mo, Y., Tian, Y., 2020. Potential linkages of precipitation extremes in Beijing-Tianjin-Hebei region, China, with large-scale climate patterns using wavelet-based approaches. *Theor. Appl. Climatol.* 141, 1251–1269. <https://doi.org/10.1007/s00704-020-03247-8>.
- Steiger, N.J., Smerdon, J.E., Seager, R., Williams, A.P., Varuolo-Clarke, A.M., 2021. ENSO-driven coupled megadroughts in North and South America over the last millennium. *Nat. Geosci.* 14 (10), 739–744. <https://doi.org/10.1038/s41561-021-00819-9>.
- Stier, P., van den Heever, S.C., Christensen, M.W., Gryspenert, E., Dagan, G., Saleaby, S.M., et al., 2024. Multifaceted AERO effects on precipitation. *Nat. Geosci.* 17 (8), 719–732. <https://doi.org/10.1038/s41561-024-01482-6>.
- Stott, P.A., Stone, D.A., Allen, M.R., 2004. Human contribution to the European heatwave of 2003. *Nature* 432 (7017), 610–614. <https://doi.org/10.1038/nature03089>.
- Treydte, K., Boda, S., Pannatier, E.G., Fonti, P., Frank, D., Ullrich, B., et al., 2014. Seasonal transfer of oxygen isotopes from precipitation and soil to the tree ring: source water vs. needle water enrichment. *New Phytol.* 202 (3), 772–783. <https://doi.org/10.1111/nph.12741>.
- Turner, A.G., Annamalai, H., 2012. Climate change and the south Asian summer monsoon. *Nat. Clim. Chang.* 2 (8), 587–595. <https://doi.org/10.1038/nclimate1495>.
- Ueda, H., Iwai, A., Kuwako, K., Hori, M.E., 2006. Impact of anthropogenic forcing on the Asian summer monsoon as simulated by eight GCMs. *Geophys. Res. Lett.* 33 (6). <https://doi.org/10.1029/2005GL025336>.
- Van Vuuren, D.P., Edmonds, J., Kainuma, M., Riahi, K., Thomson, A., Hibbard, K., et al., 2011. The representative concentration pathways: an overview. *Clim. Chang.* 109, 5–31. <https://doi.org/10.1007/s10584-011-0148-z>.
- Vuille, M., Bradley, R.S., Werner, M., Healy, R., Keimig, F., 2003. Modeling  $\delta^{18}\text{O}$  in precipitation over the tropical Americas: 1. Interannual variability and climatic controls. *J. Geophys. Res. Atmos.* 108 (D6). <https://doi.org/10.1029/2001JD002038>.
- Wang, B., Li, J., He, Q., 2017. Variable and robust East Asian monsoon rainfall response to El Niño over the past 60 years (1957–2016). *Adv. Atmos. Sci.* 34 (10), 1235–1248. <https://doi.org/10.1007/s00376-017-7016-3>.
- Wang, H., Sun, B., Yu, X., Xin, Z., Jia, G., 2020a. The driver-pattern-effect connection of vegetation dynamics in the transition area between semi-arid and semi-humid northern China. *CATENA* 194, 104713. <https://doi.org/10.1016/j.catena.2020.104713>.
- Wang, S., Chen, F., Chen, Y.P., Torbenson, M.C., Esper, J., Zhao, X., Hu, M., Zhang, H.L., Yue, W.P., Cao, H.H., 2025. Greening of Eurasia's center driven by low-latitude climate warming. *For. Ecosyst.* 100330.
- Wang, Y., Hu, C., Ruan, J., Johnson, K.R., 2020b. East Asian precipitation  $\delta^{18}\text{O}$  relationship with various monsoon indices. *J. Geophys. Res. Atmos.* 125 (13). <https://doi.org/10.1029/2019JD032282> e2019JD032282.
- Wei, J., Tang, W., Chen, F., Chen, Y., Hu, M., Wang, S., Wang, H.C., Wu, X.F., Zhang, H.L., 2025. Reduced growth of Qinghai spruce due to snow cover loss in high Asian elevations since the late 20th century. *J. For. Res.* 36 (1), 1–13.
- Wernicke, J., Grießinger, J., Hochreuther, P., Bräuning, A., 2015. Variability of summer humidity during the past 800 years on the eastern Tibetan Plateau inferred from  $\delta^{18}\text{O}$  of tree-ring cellulose. *Clim. Past* 11 (2), 327–337. <https://doi.org/10.5194/cp-11-327-2015>.
- Wu, Z.Y., Lu, G.H., Wen, L., Lin, C.A., 2011. Reconstructing and analyzing China's fifty-nine year (1951–2009) drought history using hydrological model simulation. *Hydrolog. Earth Syst. Sci.* 15 (9), 2881–2894. <https://doi.org/10.5194/hess-15-2881-2011>.

- Wu, X., Tang, W., Chen, F., Wang, S., Bakhtiyorov, Z., Liu, Y., Guan, Y., 2025. Attribution and risk projections of hydrological drought over water-scarce Central Asia. *Earth's Future* 13, e2024EF005243.
- Wyatt, M.G., 2020. Circulation patterns: Atmospheric and Oceanic. In: *Atmosphere and Climate*. CRC Press, pp. 63–90.
- Xiao, M., Zhang, Q., Singh, V.P., 2015. Influences of ENSO, NAO, IOD and PDO on seasonal precipitation regimes in the Yangtze River basin, China. *Int. J. Climatol.* 35 (12), 3556–3567. <https://doi.org/10.1002/joc.4228>.
- Xu, C., Sano, M., Nakatsuka, T., 2011. Tree ring cellulose  $\delta^{18}\text{O}$  of *Fokienia hodginsii* in northern Laos: a promising proxy to reconstruct ENSO? *J. Geophys. Res. Atmos.* 116 (D24). <https://doi.org/10.1029/2011JD016694>.
- Xu, C., Pumijumnong, N., Nakatsuka, T., Sano, M., Li, Z., 2015. A tree-ring cellulose  $\delta^{18}\text{O}$ -based July–October precipitation reconstruction since AD 1828, Northwest Thailand. *J. Hydrol.* 529, 433–441. <https://doi.org/10.1016/j.jhydrol.2015.02.037>.
- Xu, C., Sano, M., Dimri, A.P., Ramesh, R., Nakatsuka, T., Shi, F., et al., 2018. Decreasing Indian summer monsoon on the northern Indian sub-continent during the last 180 years: evidence from five tree-ring cellulose oxygen isotope chronologies. *Clim. Past* 14 (5), 653–664. <https://doi.org/10.5194/cp-14-653-2018>.
- Xu, C., Buckley, B.M., Promchote, P., Wang, S.Y.S., Pumijumnong, N., An, W., et al., 2019. Increased Variability of Thailand's Chao Phraya River Peak season Flow and its Association with ENSO Variability: evidence from tree Ring  $\delta^{18}\text{O}$ . *Geophys. Res. Lett.* 46 (9), 4863–4872. <https://doi.org/10.1029/2018GL081458>.
- Xu, Z., Han, Y., Tam, C.Y., Yang, Z.L., Fu, C., 2021a. Bias-corrected CMIP6 global dataset for dynamical downscaling of the historical and future climate (1979–2100). *Sci. Data* 8 (1), 293. <https://doi.org/10.1038/s41597-021-01079-3>.
- Xu, C., Zhao, Q., An, W., Wang, S., Tan, N., Sano, M., et al., 2021b. Tree-ring oxygen isotope across monsoon Asia: Common signal and local influence. *Quat. Sci. Rev.* 269, 107156. <https://doi.org/10.1016/j.quascirev.2021.107156>.
- Xu, C., Wang, S.Y.S., Borhara, K., et al., 2023a. Asian-Australian summer monsoons linkage to ENSO strengthened by global warming. *npj Clim Atmos Sci* 6, 8. <https://doi.org/10.1038/s41612-023-00341-2>.
- Xu, H., Wang, T., Wang, H., 2023b. Interdecadal Pacific Oscillation responsible for the linkage of decadal changes in precipitation/moisture in arid Central Asia and humid Asian monsoon region during the last millennium. *Clim. Past Discuss.* 2023, 1–39. <https://doi.org/10.5194/cp-20-107-2024>.
- Yang, B., Qin, C., Wang, J., He, M., Melvin, T.M., Osborn, T.J., Briffa, K.R., 2014. A 3,500-year tree-ring record of annual precipitation on the northeastern Tibetan Plateau. *Proc. Natl. Acad. Sci.* 111 (8), 2903–2908. <https://doi.org/10.1073/pnas.1319238111>.
- Yang, J., Cooper, D.J., Li, Z., Song, W., Zhang, Y., Zhao, B., et al., 2020. Differences in tree and shrub growth responses to climate change in a boreal forest in China. *Dendrochronologia* 63, 125744. <https://doi.org/10.1016/j.dendro.2020.125744>.
- Yang, B., Qin, C., Bräuning, A., Osborn, T.J., Trouet, V., Ljungqvist, F.C., et al., 2021. Long-term decrease in Asian monsoon rainfall and abrupt climate change events over the past 6,700 years. *Proc. Natl. Acad. Sci.* 118 (30). <https://doi.org/10.1073/pnas.2102007118> e2102007118.
- Yao, C., Yang, S., Qian, W., Lin, Z., Wen, M., 2008. Regional summer precipitation events in Asia and their changes in the past decades. *J. Geophys. Res. Atmos.* 113 (D17). <https://doi.org/10.1029/2007JD009603>.
- Yu, J., Li, Q., Ding, Y., Wen, Z., Gong, Z., Sun, X., et al., 2024. AMO modulation of interdecadal background of persistent heavy rainfall in summer over the Huaihe River Basin. *Clim. Dyn.* 62 (5), 3621–3640. <https://doi.org/10.1007/s00382-023-07088-9>.
- Yue, W., Chen, F., Torbenson, M.C.A., Zhao, X., Zheng, Y., Xu, Y., Hu, M., Wang, S., Hou, T., Zhang, H., Chen, Y., 2024. Late Ming Dynasty weak monsoon induced a harmonized megadrought across North-to-South China. *Commun. Earth Environ.* 5, 439.
- Zhang, R., 2015. Changes in East Asian summer monsoon and summer rainfall over eastern China during recent decades. *Sci. Bull.* 60 (13), 1222–1224. <https://doi.org/10.1007/s11434-015-0824-x>.
- Zhang, Y., Zhou, W., Wang, X., Wang, X., Zhang, R., Li, Y., Gan, J., 2022a. IOD, ENSO, and seasonal precipitation variation over Eastern China. *Atmos. Res.* 270, 106042. <https://doi.org/10.1016/j.atmosres.2022.106042>.
- Zhang, Y., Wang, W., Ding, R., Li, J., Sun, C., 2022b. Modulation of the predictability of the East Asian summer monsoon by the interdecadal Pacific oscillation. *J. Geophys. Res. Atmos.* 127 (16). <https://doi.org/10.1029/2021JD035903> e2021JD035903.
- Zhao, X., Fang, K., Chen, F., Martín, H., Roig, F.A., 2023. Reconstructed Jing River streamflow from western China: a 399-year perspective for hydrological changes in the Loess Plateau. *J. Hydrol.* 621, 129573. <https://doi.org/10.1016/j.jhydrol.2023.129573>.
- Zhao, C., Sun, Y., Yang, J., Li, J., Zhou, Y., Yang, Y., et al., 2024. Observational evidence and mechanisms of AERO effects on precipitation. *Sci. Bull.* <https://doi.org/10.1016/j.scib.2024.03.014>.
- Zhou, T.J., Yu, R.C., 2005. Atmospheric water vapor transport associated with typical anomalous summer rainfall patterns in China. *J. Geophys. Res. Atmos.* 110 (D8). <https://doi.org/10.1029/2004JD005413>.
- Zhou, S., Yu, B., Zhang, Y., 2023. Global concurrent climate extremes exacerbated by anthropogenic climate change. *Science. Advances* 9 (10), eab01638.